JOURNAL OF PETROLOGY | VOLUME 52 | NUMBER 10 | PAGES 1987–2008 | 2011 | doi:10.1093/petrology/egr037

Open-system Behavior during Pluton–Wall-rock Interaction as Constrained from a Study of Endoskarns in the Sierra Nevada Batholith, California

BLAKE DYER[1†], CIN-TY A. LEE[1]*, WILLIAM P. LEEMAN[1‡] AND MICHAEL TICE[2]

[1]DEPARTMENT OF EARTH SCIENCE, MS-126, RICE UNIVERSITY, 6100 MAIN ST., HOUSTON, TX 77005, USA

[2]DEPARTMENT OF GEOLOGY AND GEOPHYSICS, MS 3115, COLLEGE STATION, TX 77843, USA

RECEIVED OCTOBER 17, 2009; ACCEPTED JULY 4, 2011
ADVANCE ACCESS PUBLICATION AUGUST 12, 2011

Crustal xenoliths (pyroxenites and plagioclase + quartz + pyroxene lithologies) from the Quaternary Big Pine volcanic field on the eastern flank of the Sierra Nevada Batholith in California (USA) represent the products of metasomatic reaction between the margins of a Cretaceous granodioritic pluton and Paleozoic marbles, possibly at mid-crustal depths based on the equilibration temperatures recorded by Ti-in-quartz geothermometry. This interpretation is based on the presence of plagioclase showing relict plutonic textures, pyroxenite characterized by nearly pure diopside clinopyroxene, recrystallized plagioclase with anomalously high anorthite content, textures indicating replacement of plagioclase by clinopyroxene (and vice versa), 'ghost' plagioclase rare earth element signatures in some clinopyroxenes, and the presence of phlogopite endmember micas at the contact between clinopyroxene-rich and plagioclase-rich zones. These observations suggest that the xenoliths represent fragments of an 'endoskarn', the outer sheath of a pluton that chemically reacted with carbonate country-rock. Mass transfer between the carbonate country-rock and the pluton involved transfer of Ca and Mg from the carbonate into the pluton and transfer of Na, K, Al and Si from the pluton to the carbonate, the latter generating extensive endoskarns. The Ca metasomatism of the pluton converted alkali feldspar components into anorthite-rich plagioclase, releasing Na and K, which left the plutonic system. K, in particular, migrated towards the carbonate and precipitated phlogopite upon entering clinopyroxene-rich lithologies. Mass-balance calculations, based on theory and residual enrichments in immobile elements such as Ti, suggest that the pluton experienced net mass loss (>15%) in the form of Si, Al, Na and K to the surrounding country-rock, but a net gain in Ca and Mg.

KEY WORDS: *skarn; endoskarn; pluton; assimilation; carbonate; diopside*

INTRODUCTION

Assimilation of wall-rock can be an important process in the compositional evolution of a magma body (DePaolo, 1981; Bohrson & Spera, 2001; Spera & Bohrson, 2001). The simplest type of assimilation involves direct physical entrainment of the wall-rock (i.e. stoping) followed by homogenization within the magma chamber. More complicated scenarios of magma differentiation include assimilation coupled with fractional crystallization and magma recharge (DePaolo, 1981; Bohrson & Spera, 2001; Spera & Bohrson, 2001) or selective assimilation of partial melts derived from the wall-rock (Mills *et al.*, 2009). Here, we focus on a different aspect of crustal assimilation, namely reactive wall-rock assimilation, where the outer margins of a magma body chemically and thermally interact with the wall-rock. Such processes often involve mass exchange via fluids, which are the media for transporting various

*Corresponding author. Telephone: 281-250-3606.
E-mail: ctlee@rice.edu
†Present address: Department of Geosciences, Princeton University, Guyot Hall, Washington Road, Princeton, New Jersey 08544, USA
‡Present address: National Science Foundation, Earth Science Division, 4201 Wilson Blvd., Arlington, VA 22230, USA

elements down chemical potential gradients across the wall-rock–pluton contact. Hydrothermal fluids emanating from the pluton can give rise to extensive mineralization zones in the country-rock, generating ore and skarn deposits in an outer metasomatic aureole (Lindgren, 1933). Reverse migration of fluids or certain elements, that is, from the wall-rock into the magma, can also occur provided the chemical potential gradient is directed towards the magma (Lindgren, 1933). In such scenarios, the inner margins of the magma body may become extensively metasomatized (Fulignati *et al.*, 2004). This inner metasomatic aureole is often referred to as an endoskarn (because it is in the magma body itself) whereas the outer (wall-rock) metasomatic aureole is the exoskarn (Fulignati *et al.*, 2004).

Reactive interaction of magmas with their country-rocks has broad implications. Generation of new continental crust often involves the interaction of juvenile magmas with pre-existing lithosphere, such as in continental arcs. In addition, interaction with volatile-bearing country-rocks, such as carbonate-bearing sediments, could lead to extensive devolatilization via decarbonation reactions. This has implications for volcanic degassing and climate change. Thus, of interest here is how reactive assimilation can be detected. Magmas undergoing reactive assimilation should evolve differently from magmas undergoing direct wall-rock assimilation. In element–element mixing diagrams, reactive wall-rock assimilation will result in non-linear mixing arrays, unlike direct wall-rock assimilation, which is linear. Of course, any magmatic recharge, fractional crystallization, diffusive decoupling or selective assimilation of wall-rock will impart a level of nonlinearity to the system (DePaolo, 1981; Lesher, 1990). We are particularly interested in magma–wall-rock interactions at mid-crustal depths because the extent of such reactions is probably greater than at shallower depths of intrusion because the wall-rock is warmer (DePaolo *et al.*, 1992; Hammersley & DePaolo, 2006). For this study we investigated crustal xenoliths exhumed in the Pleistocene Fish Springs alkali basalt cinder cone in the Big Pine volcanic field on the eastern front of the Sierra Nevada, California (Fig. 1). The Fish Spring cone erupted on the southern margin of a Cretaceous granodiorite pluton (the Tinemaha granodiorite), which itself was intruded through Paleozoic metasedimentary units. We focus here on a suite of petrogenetically related xenoliths, consisting of pyroxene-rich, pyroxene + plagioclase, and pyroxene + plagioclase + quartz lithologies, which we interpret to represent endoskarns associated with reaction between a granodioritic pluton and dolomitic country-rock. Although there are already numerous studies of pluton–wall-rock interaction, most of these have focused on the macro-scale. Here, we examine the mineralogical and geochemical evolution of wall-rock reaction at the centimeter-scale to better understand the petrogenetic processes governing the reaction.

GEOLOGICAL BACKGROUND

The Quaternary Big Pine volcanic field (0·1–0·5 Ma) consists of ~0·5 km^3 of basaltic lava flows and cinder cones (~40), erupted through normal faults along the eastern front of the Sierra Nevada and the western flank of Owens Valley near the towns of Big Pine and Independence (Ormerod *et al.*, 1988; Bierman *et al.*, 1991; Beard & Glazner, 1995; Mordick & Glazner, 2006; Blondes *et al.*, 2008; Fig. 1). A few cones and lava flows also erupted on the east flank of Owens Valley. Basement rocks to the west of the volcanic field are largely made up of Cretaceous granitoids (Bateman, 1961; Kistler *et al.*, 1965; Sawka *et al.*, 1990), whereas Paleozoic metasedimentary rocks lie to the east; thus the Big Pine volcanic field straddles the transition between these basement lithologies (Lackey & Valley, 2004). Most of the basalts fall in the alkali basalt field and range from primitive (>10 wt % MgO) to moderately evolved (6 wt % MgO) compositions (Mordick & Glazner, 2006; Blondes *et al.*, 2008). The most primitive magmas contain xenoliths of spinel lherzolite (Beard & Glazner, 1995; Ducea & Saleeby, 1996; Lee *et al.*, 2001). The inferred parental liquid compositions of these primitive magmas suggest last equilibration with the mantle at ~1350°C and at pressures between 1·5 and 2·0 GPa (Wang *et al.*, 2002; Lee *et al.*, 2009*a*). Clinopyroxene–liquid barometry indicates that crystallization of the most primitive magmas began at depth, between 1·2 and 1·7 GPa and hence within the mantle, leaving little time between melt generation, crystallization and eruption, implying that the magma ascent rate from the mantle source to the surface was rapid (Mordick & Glazner, 2006). In contrast, the more evolved basalts, which host the crustal xenoliths investigated here, indicate clinopyroxene crystallization pressures between 0·8 and 1·1 GPa, suggesting that these magmas stalled and crystallized within the crust (Mordick & Glazner, 2006). These cinder cones do not contain mantle xenoliths, but instead contain abundant crustal xenoliths.

In this study we focus on crustal xenoliths from the 0·314 Ma Fish Springs cinder cone (N 37·0712, W 118·2550). The Fish Springs cone is one of the more evolved and probably crustally contaminated basalts (SiO_2 52·91 wt %, MgO 6·35 wt %; Martel *et al.*, 1987; Zehfuss *et al.*, 2001; Mordick & Glazner, 2006; Blondes *et al.*, 2008; Fig. 1). The cinder cone erupted through the southern margin of the mid-Cretaceous Tinemaha granodiorite dated at 123 Ma (Kistler *et al.*, 1965; Sawka *et al.*, 1990). Paleozoic carbonates, in the form of roof pendants, are abundant in the Sierra Nevada batholith in the vicinity of Big Pine and also in the Inyo and White Mountains to the east (Sylvester, 1969; Kerrick, 1970, 1977; Brock, 1972;

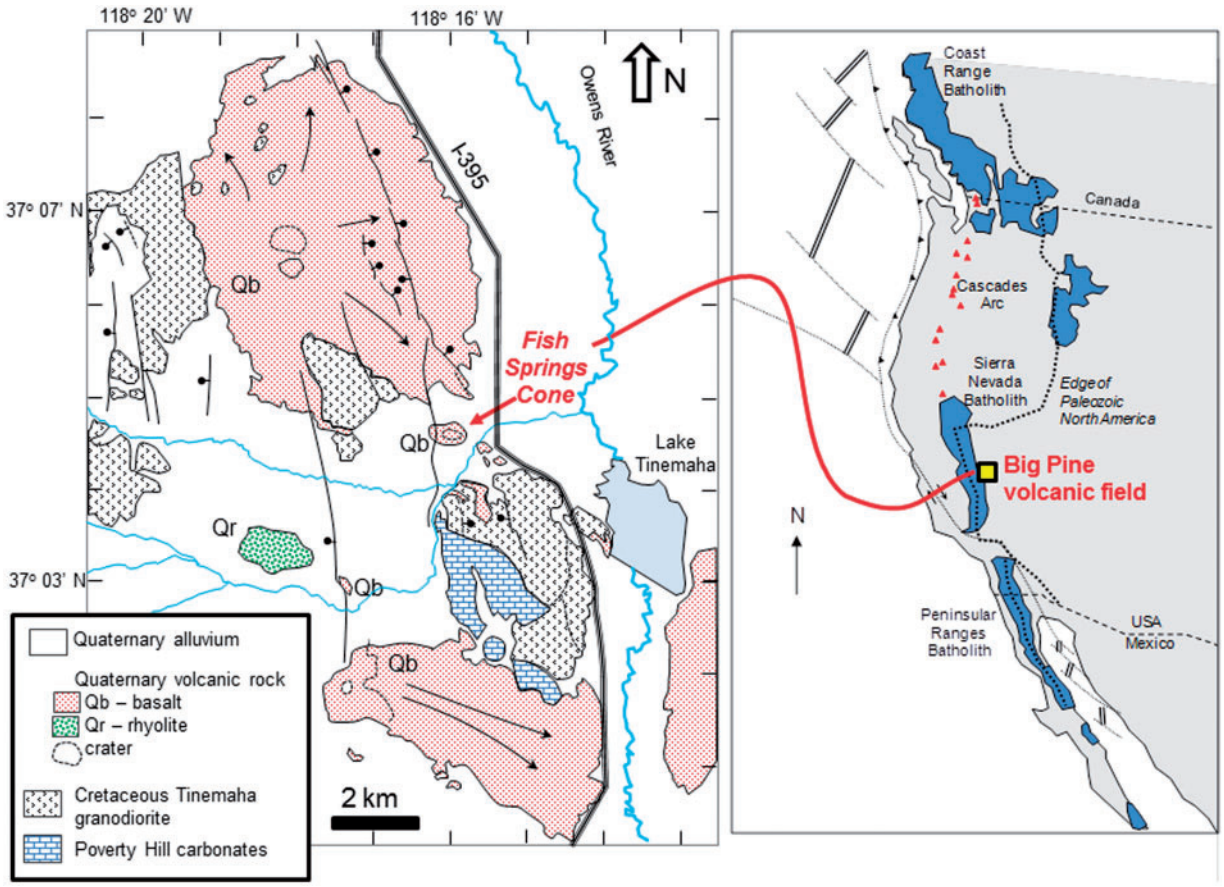

Fig. 1. Map (left) of part of the Big Pine volcanic field (Bateman *et al.*, 1963; Nelson, 1966), showing the location of the Fish Springs cinder cone. Right-hand map shows where the Big Pine volcanic field lies in relation to the Cretaceous Sierra Nevada Batholith in California. The Paleozoic Poverty Hills marble unit lies 2 km south of Fish Springs. The Fish Springs magma erupted through the Tinemaha granodiorite pluton.

Gans, 1974; Miller, 1975; Wright *et al.*, 1978; Moore & Foster, 1980; Greene & Stevens, 2002; Lackey & Valley, 2004). Most of the carbonates in the Sierra Nevada are limestones, including the Paleozoic Poverty Hills marble complex, which lies 2 km south of Fish Springs. The skarns here are diopside–epidote–grossular–carbonate rocks. However, Paleozoic dolomites lie just east of Big Pine in the Inyo and White Mountains, such as those near the Papoose Flat pluton (Sylvester, 1969). Many of the margins of the roof-pendants have been contact-metamorphosed by the granitoid plutons, resulting in extensive skarnification and formation of hornfels. Most of the contact zones in the eastern Sierra represent shallow-level processes because plutons in the eastern Sierras have experienced only moderate exhumation (Ague & Brimhall, 1988*a*). Some of these shallow-level contacts in the form of roof pendants have been investigated petrologically and geochemically (Kerrick, 1970, 1977; Brock, 1972; Hanson *et al.*, 1993; Lackey & Valley, 2004; Lackey *et al.*, 2008). In contrast, deep-level (>1 GPa) interaction of magmas with metasedimentary country-rocks is exposed in the southern Sierras, where deeper parts of the batholith appear to have been exhumed (Pickett & Saleeby, 1993). However, these deep-seated metasediments have not yet been studied petrologically in detail. The purpose of this study is to use xenoliths as a means of sampling the deep crust beneath the eastern Sierra Nevada.

XENOLITH DESCRIPTIONS AND PETROGRAPHY

Xenoliths in the Fish Springs cone are abundant in exposed cliff faces of a quarry on the east flank as well as a naturally eroded bank on the NE side of the cone. The xenolith suite includes augite–plagioclase gabbros, granodiorites, and a distinctive subset of related lithologies characterized by diopsidic pyroxene, plagioclase and quartz. The augite–plagioclase gabbros are likely derived from cumulates from basaltic magmas associated with the Big Pine volcanic field. The granodiorite xenoliths are

Table 1: Modal mineralogy of representative lithologies

Rock type			Modes				Accessory minerals	Texture
			px	Plag	qz	phlog		
Pyroxenite								
L03-3			0·9	0·1			Fe-oxide	granular
L03-6			1					granular
L03-10			1					granular
L03-18			1					granular
L03-26			0·85	0·15			Fe-oxide	granular
Plagioclase–quartz–pyroxene								
L03-15			0·3	0·6	0·1			sheared
Composite								
L03-4	Lithology 1	plag + qz + px		0·8	0·2		titanite, zircon	granular
	Lithology 2	px	1				Fe-oxide	granular
	Lithology 3	phlog				1	Fe-oxide	granular
L03-8	Lithology 1	plag + qz + px	0·05	0·8	0·15	0·15	titanite, zircon	granular
	Lithology 2	px + plag	0·95	0·05			phlogopite, Fe-oxide	granular

probably derived from the Tinemaha granodiorite pluton. Most of the granodiorite xenoliths appear to have experienced 'flash-heating' during entrainment in the basaltic host magma, leading to preferential melting and extraction of low melting point phases such as biotite and hornblende. The melting-out of these phases has left behind a porous rock that retains the rock's original structure supported by relict quartz and feldspar grains that did not melt significantly. These lithological groups, although interesting, are not considered further here.

The main focus of this study is on the pyroxene–plagioclase–quartz lithologies, to which we refer subsequently as 'endoskarns', following the terminology of Kerrick (1977). The endoskarn xenoliths are angular fragments that approach 20 cm in the longest dimension. Unlike the granodiorite xenoliths, the endoskarn group shows no evidence for melting associated with interaction with the host basalt. It also shows no evidence for post-eruption alteration. The endoskarn xenoliths can be categorized into three groups: a pyroxenite group, a plagioclase + quartz ± pyroxene group, and a composite group that contains the first two lithologies in contact relationship. We describe their petrography below. Mineral modes are given in Table 1.

Pyroxenite group

The pyroxenite group is composed of >85% bottle-green diopsidic clinopyroxene with the remaining mode as plagioclase and minor accessory oxides (<1%). The pyroxenite group exhibits a continuum in textures. One extreme is characterized by a fine- to medium-grained equigranular mosaic texture (Fig. 2a). None of the grains show unbounded crystal faces and most grain boundaries appear to have undergone subsolidus re-equilibration without deformation as evidenced by pervasive 120° triple junctions and the random crystallographic orientation of the mineral grains (e.g. no lattice-preferred orientation). Pyroxenes in this textural type show no evidence of exsolution. Plagioclase grains tend to be smaller than the pyroxene grains and most show no obvious twinning, perhaps owing to their small size. In one sample, L03-3, pyroxene replaces plagioclase, as can be seen in Fig. 2a, where optically continuous plagioclase grains are interrupted by pyroxene grains. We believe this texture to be related to subsolidus metamorphic reactions rather than a magmatic feature owing to the equigranular texture of this rock. The other extreme is characterized by medium- to coarse-grained (>5 mm but up to 1 cm) pyroxenes and minor (0 to <5%), plagioclase crystals. Grain-size distribution is heterogeneous, as are grain shapes. The overall texture is that of sub-prismatic coarse-grained pyroxene crystals growing in an interlocking manner, reminiscent of an igneous cumulate texture. These pyroxenes rarely show exsolution lamellae, but they show much better defined cleavage than the pyroxenes in the rocks with equigranular texture. A curious feature is that these coarse-grained pyroxenes often occur in 'composite' xenoliths where two different lithological groups

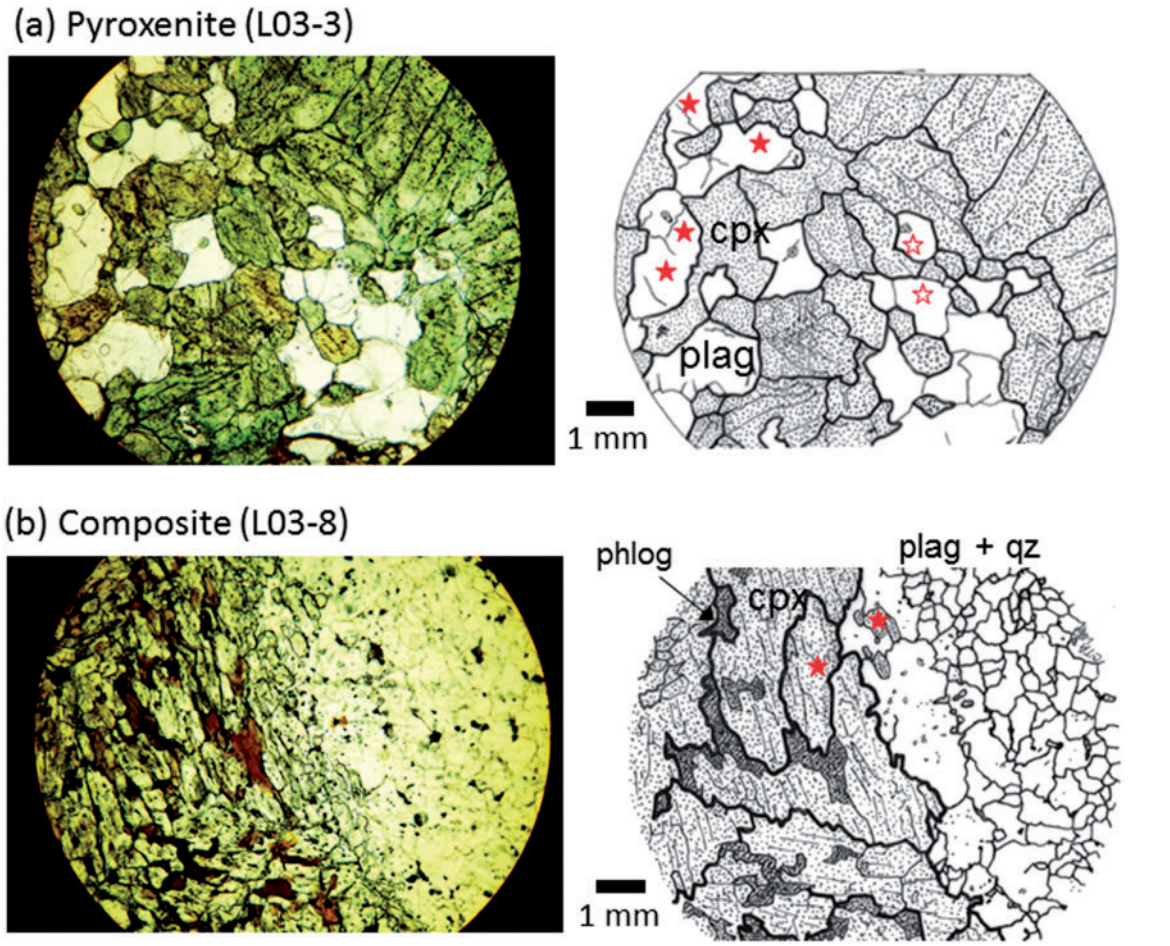

Fig. 2. (a) Photomicrograph and interpretative sketch of pyroxenite textures. Dark stippled grains are pyroxenes (cpx); white grains are plagioclase (plag). Bold lines are used to demarcate the boundaries of optically continuous grains. In the case of plagioclase, optically continuous grains are denoted by paired symbols (open or filled stars). (b) View of the contact relationship between pyroxenite and felsic lithologies (photomicrograph and interpretative sketch). Very dark stippled grains are phlogopite (phlog); moderately stippled grains are pyroxenes; white areas are plagioclase or quartz (qz). Bold lines again define optically continuous grains as do paired stars. It should be noted that plagioclase grains in this sample differ from those in (a) by the abundance of fluid inclusions, which are represented as dots or tiny blebs in (b).

are juxtaposed (see below). Fluid inclusions are abundant in the pyroxenites, but most of the fluid inclusions are <100 μm and occur along healed fractures, suggesting that they may be related to the host magma itself.

Plagioclase + quartz ± pyroxene group

This group (Figs 2b, 3a–d and 4a) is dominated by plagioclase (>50–80%), followed by quartz (20–50%) and sometimes diopsidic clinopyroxene (0–15%). In hand sample, these lithologies are white, granular rocks that locally contain fine bands of clinopyroxene, which define a foliation. In thin section, the texture is best described as transitional between a sheared (with shape-preferred orientation) and an equigranular texture (Fig. 3a). Plagioclase grains are elongated in the plane of foliation with aspect ratios of 3–5. Optically continuous grains also appear to have grown parallel to the foliation. In most samples, the plagioclases are so fine-grained that they show minimal twinning. Pyroxene grains are mostly equigranular in shape, but often occur as elongate clusters that define the macroscopic foliation (Fig. 3a); these clusters may represent the dismembered remnants of originally larger pyroxene grains. Quartz occurs primarily as equigranular grains distributed throughout the rock. There is also an abundance of accessory minerals, such as titanite and zircon (Fig. 3c and d). Titanite occurs as fine- to medium-grained (up 2 mm) euhedral crystals at up to 5–10% of the mode. Zircon grains are <200 μm and euhedral and in some places abundant (5 zircons per mm^2).

Although most of the samples in this xenolith category have metamorphic deformation textures, relict igneous textures are present in some of the samples (Fig. 3a and b). These textures are characterized by medium- to coarse-grained plagioclase crystals that show extensive

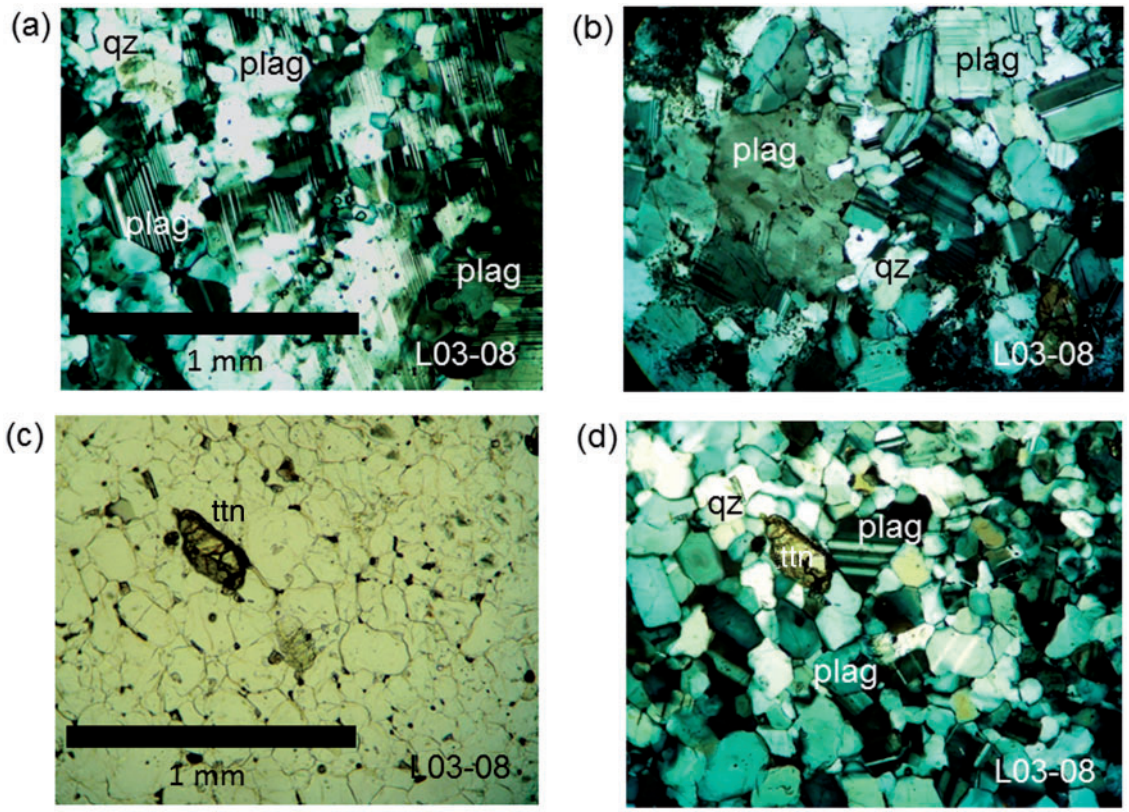

Fig. 3. Photomicrographs of plagioclase + quartz ± pyroxene lithologies. (a) Crossed polars, showing large, optically continuous plagioclase grain (the grain showing extensive twinning lamellae) surrounded and embayed by much smaller recrystallized plagioclase grains. (b) Crossed polars, showing relict igneous texture of plagioclase and quartz grains. The interlocking, subhedral plagioclase grains should be noted. (c) Plane-polarized light; plagioclase + quartz lithology showing a metamorphic recrystallization texture and large titanite grain. (d) Same as (c) but under crossed polars. plag, plagioclase; qz, quartz; phlog, phlogopite; cpx, clinopyroxene; ttn, titanite.

albite twinning and interlocking relationships with neighboring plagioclase grains, both of which are common features seen in plutonic rocks. Locally, some of these relict igneous grains have recrystallized into equigranular plagioclase grains, showing little to no twinning. For example, as can be seen from Fig. 3a, large (1 mm) optically continuous plagioclase grains 'engulf' finer-grained (<0·1 mm) equigranular plagioclase grains. This texture superficially resembles a poikilitic cumulate texture, but because the grain boundaries between the large plagioclase grains and the smaller plagioclase grains are gradational (as can be seen under crossed polars), we interpret this as a recrystallization texture. The abundance of quartz in these lithologies indicates that the protolith was a granodiorite rather than a more mafic magmatic rock, such as diorite or gabbro.

Composite relationships between different groups

Because of the large size of some of the xenoliths, composite relationships between the different groups are occasionally preserved. The most distinctive composite xenoliths are those in which the felsic lithologies (plagioclase–quartz–diopside group) are juxtaposed against the pyroxenite (Figs 4b and 5). In hand sample, the contact between the two lithologies is sharp. In some cases, this boundary is straight but more commonly the contact is undulating because the felsic lithology intrudes into the pyroxenite, sometimes generating finger-like veins and embayments. Phlogopite is almost always associated with these contacts (Figs 4b and 5), but occurs primarily in the pyroxenite and only sparsely in the felsic parts. Small magnetite grains (white areas in Fig. 5) occur primarily in and near the phlogopite zones. The plagioclase grain size increases toward the contact (Fig. 2b). Blebs of pyroxene occur within the felsic lithology near the contact. Those closest to the boundary are optically continuous with the pyroxenes in the pyroxenite, suggesting local replacement of pyroxene by plagioclase as seen in Fig. 2b (it should be noted that this is the reverse of what is seen in the pyroxenites as described above). Much of the contact appears to be recrystallized, and the grains do not show any preferred crystallographic orientation. Combined with the preservation of optically continuous blebs of pyroxene, these

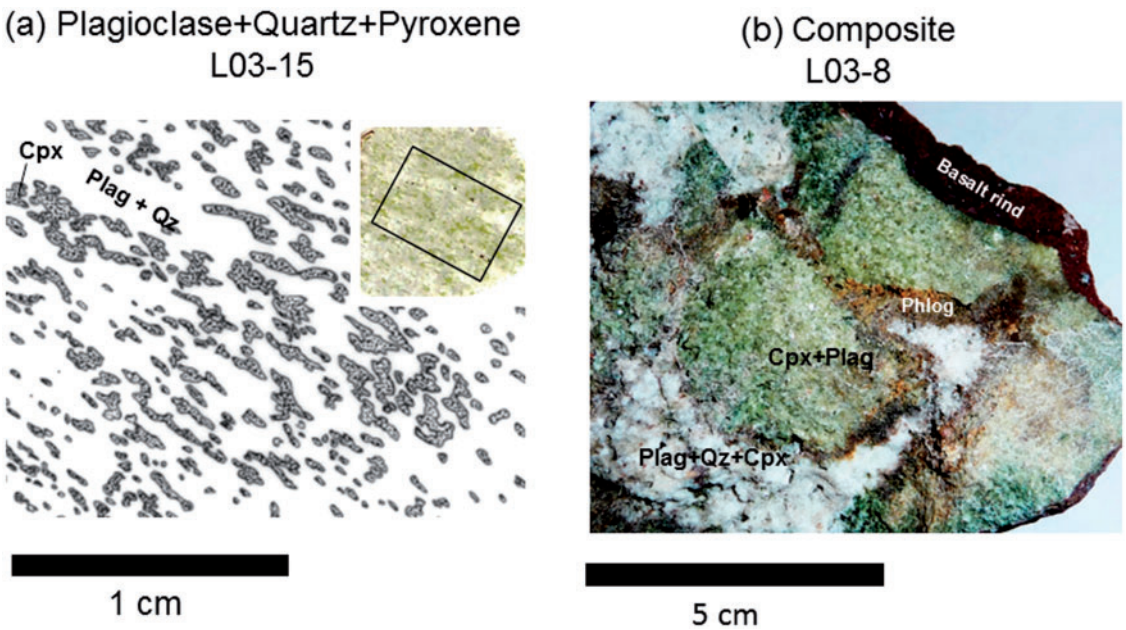

Fig. 4. Macroscopic textural features. (a) Plagioclase + quartz + pyroxene lithology. Pyroxenes (dark stippled grains) are arranged as disaggregated blebs that define a weak macroscopic foliation. White areas represent quartz and plagioclase. Grain sizes are too small to sketch. (b) Hand specimen-scale view of the contact relationship between the felsic (plagioclase + quartz + pyroxene) lithology and pyroxenite. The embayed contact relationship and the localization of phlogopite to the contact itself should be noted. Plag, plagioclase; Qz, quartz; Phlog, phlogopite; Cpx, clinopyroxene.

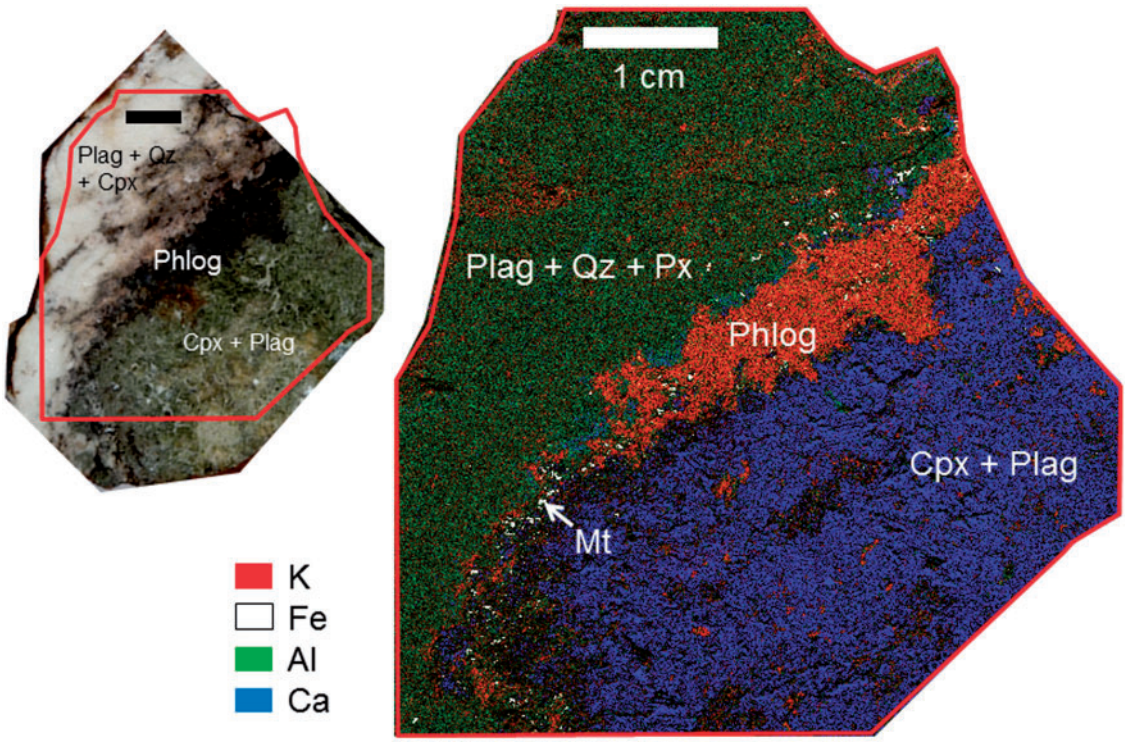

Fig. 5. False-color micro-XRF map at a 100 μm spatial resolution of a composite xenolith, showing the textural and compositional relationship between an endoskarn (granodiorite protolith) and a clinopyroxene and phlogopite reaction zone. Plag, plagioclase; Qz, quartz; Phlog, phlogopite; Px, clinopyroxene; Mt, magnetite.

observations indicate that the contact itself underwent little subsolidus deformation. Finally, an important feature in these composite xenoliths is the abundance of large spherical fluid inclusions (up to 300 μm). Unlike those fluid inclusions seen in the pyroxenites, these fluid inclusions are not in healed fractures but occur as lone inclusions within plagioclase crystals or as spherical inclusions at intergranular triple junctions (Fig. 2b). These textural features indicate that these fluid inclusions predate entrainment of the xenolith into the host basalt.

ANALYTICAL METHODS

Major and trace element concentrations were determined by laser ablation inductively coupled plasma mass spectrometry (LA-ICP-MS) using a New Wave 213 nm laser and a ThermoFinnigan Element 2 magnetic sector ICP-MS system. Major elements and some minor and trace elements were determined in medium mass resolution mode ($m/\Delta m = 3000$) to resolve isobaric interferences (mainly argides and oxides). Trace elements without significant isobaric interferences were measured in low mass resolution mode ($m/\Delta m = 300$) to ensure maximum sensitivity. Drift of magnet was corrected by using the 'lock mass' option on the $^{40}Ar^{40}Ar$ dimer. The laser was run at a 55 μm spot size, 10 Hz pulse frequency, and an energy density per pulse of 19 J cm^{-2}. Ablated material was flushed and introduced into the quartz torch using 1·3 l min^{-1} flow of helium gas, coupled with 0·9 l min^{-1} argon sample gas flow. All ablation analyses were preceded by a 10 s gas background, which was subtracted from the ablation signal. Conversion of signals into concentrations made use of external calibration curves based on analyses of USGS glass standards, BHVO-2 g, BIR1g, and BCR-2 g using preferred values from Gao *et al.* (2002). Major element concentrations were determined from medium mass resolution measurements without the need for an internal standard. This was done by assuming all metals are in the oxide form and summing to 100%, following the methods outlined by Lee *et al.* (2009*b*). Mg (for pyroxenes) or Ca (for plagioclase) concentrations determined in this way were used as internal standards for separate low mass resolution measurements following standard protocols for data reduction (Longerich *et al.*, 1996). For quartz, only medium mass resolution measurements were made. Detection limits were defined as three times the standard deviation of the gas background normalized to signal sensitivity. Only data above the detection limit are reported.

We also conducted a micro-X-ray fluorescence (XRF) scan of one of the composite samples (Fig. 5) using a Horiba Jobin Yvon XGT-7000 energy-dispersive XRF microscope with a rhodium target at Texas A&M University. Analyses were conducted using a 50 kV accelerating voltage, a 1 mA current, and 100 μm spot size. Average dwell time per spot was 0·06 s, and dead time was <20%. Results of Kα lines for K, Fe, Al, and Ca are shown in Fig. 5.

RESULTS

Mineral chemistry

Mineral compositions are reported in Tables 2–5. Pyroxene compositions lie almost exactly on the diopside–hedenbergite join (Fig. 6a). With the exception of L03-3, which has an Mg-number [molar Mg/(Mg + total Fe)] of 0·56, pyroxene Mg-numbers range from 0·76 to 0·92, indicating that some of them are nearly pure diopside. The Na_2O and Al_2O_3 contents of the pyroxene are low, in the range of 0·13–0·3 and 0·45–0·83 wt %, respectively. L03-3 pyroxenite shows textural evidence for replacement of plagioclase by pyroxene, and has the highest Na_2O (0·3 wt %) and Al_2O_3 (0·83 wt %) contents observed. Plagioclase has anorthite contents ranging between 40 and 70, thus ranging between andesite and bytownite (Fig. 6b). These anorthite contents are significantly higher than those of the plagioclase that occurs in typical granodiorites, which have An < 50 (Ernst, 1976). Mica was analyzed only in L03-8 (Table 4). Mica composition falls in the range of phlogopite.

Trace element chemistry

Pyroxene

Pyroxene trace-element contents (Table 2) normalized to primitive mantle values (McDonough & Sun, 1995) are shown in Fig. 7a. We have plotted the sequence of elements following the convention of increasing compatibility during anhydrous mantle melting and the generation of basalts (Hofmann, 1988). This does not imply that the elemental abundances in the endoskarns are controlled by the same processes as those during mantle melting. However, plotted in this order, any elemental fractionation processes deviating from that expected for mantle melting will be revealed as an anomaly in the normalized abundance pattern.

The pyroxene normalized trace element abundance patterns are roughly sub-parallel, indicating similar elemental fractionation mechanisms. However, absolute abundances vary by up to a factor of 10 between rock samples and even within the same rock sample (Fig. 7a). As can be seen in Table 2, the standard deviation for different pyroxene grains is 30% for many of the trace elements, in excess of analytical uncertainties (~5–10%). The trace-element abundance patterns of these pyroxenes do not resemble those of typical igneous pyroxenes, which generally show monotonically increasing or decreasing rare earth element (REE) profiles when plotted in order of increasing compatibility, atomic number or cation radius. The pyroxenes in this study show an overall light REE (LREE) enrichment pattern, but La is less enriched than Ce, which causes a Ce hump in the REE abundance

Table 2: Pyroxene compositions in xenoliths

Major elements	MR	Pyroxenite										Plag + Qz + Px		Composite (Plag + Px)	
		L03-3		L03-6		L03-10		L03-18		L03-26		L03-15		L03-8	
		Av. $n=10$	SD	Av. $n=3$	SD	Av. $n=3$	SD	Av. $n=3$	SD	Av. $n=3$	SD	Av. $n=12$	SD	Av. $n=9$	SD
wt %															
SiO_2	Si28	51·13	2·03	53·74	0·97	53·45	2·87	53·97	1·11	53·92	2·31	53·08	3·72	53·85	1·41
TiO_2	Ti49	0·021	0·01	0·02	0·01	0·03	0·02	0·03	0·01	0·03	0·01	0·05	0·06	0·02	0·01
Al_2O_3	Al27	0·85	0·67	0·50	0·14	0·96	0·62	0·53	0·10	0·71	0·11	0·81	0·19	0·53	0·23
FeO	Fe57	13·54	0·74	3·34	1·61	3·13	0·45	2·62	1·36	3·69	0·44	8·13	2·18	4·22	1·49
MgO	Mg25	9·60	0·61	16·75	1·49	17·38	1·61	18·09	2·07	16·97	1·60	14·53	2·13	16·57	1·38
MnO	Mn55	0·94	0·14	1·52	0·23	0·17	0·03	0·69	0·35	0·19	0·03	0·39	0·13	0·26	0·08
CaO	Ca43	23·65	1·37	24·04	1·15	24·68	1·60	23·94	1·19	24·15	1·12	22·80	2·01	24·41	1·55
Na_2O	Na23	0·29	0·05	0·12	0·05	0·23	0·15	0·16	0·04	0·37	0·05	0·26	0·07	0·16	0·04
P_2O_5	P31	0·0050	0·0053	0·0013	0·0001	0·0029	0·0023	0·0024	0·0009	0·0153	0·0210	0·0047	0·0021	0·0048	0·0012
Total		100		100		100		100		100		100		100	
Mg-no.		0·558		0·899		0·908		0·925		0·891		0·761		0·875	

Trace elements	LR	Av. $n=4$	SD	Av. $n=3$	SD	Av. $n=3$	SD	Av. $n=3$	SD	Av. $n=3$	SD	Av. $n=5$	SD	Av. $n=3$	SD
ppm															
Li	Li7	21	3·3	9·8	2·8	0·7	0·6	13·4	3·1	13	2	50	7	6·8	0·8
Cr	Cr53	5·2	1·2	8·8	1·4	4·0	2·0	2·5	1·1	22	5	31	4	4·0	1·5
Co	Co59	22	3·74	7·0	3·9	6·1	0·31	5·7	1·6	20	5	16	0·6	4·1	1·1
Ni	Ni60	30	3·03	5·8	3·4	3·6	0·26	5·3	0·93	28	1	9·4	0·4	4·5	0·3
Zn	Zn66	390	23	77	53	107	48	77	22	n.a.	n.a.	174	10	65	27
Rb	Rb85	1·7	0·52	0·31	0·10	0·9	1·1	0·41	0·06	0·31	0·44	0·15	0·21	0·34	0·16
Sr	Sr88	17	2·0	24	1·2	35	2	24	4·6	102	16	7·8	1·2	14·6	3·2
Y	Y89	0·21	0·08	4·4	0·9	8·3	0·19	5	2·8	25	10	8·5	2·3	3·1	0·40
Zr	Zr91	6·37	3·23	3·7	1·4	2·43	0·02	4·0	1·6	21	14	5·1	1·5	2·4	0·75
Nb	Nb93	0·02	0·01	0·027	0·01	0·089	0·10	0·024	0·004	0·075	0·073	0·012	0·009	0·087	0·03
Cs	Cs133	0·93	0·20	0·018	0·022	0·027	0·04	0·03	0·02	0·046	0·062	0·017	0·016	0·15	0·09
Ba	Ba137	3·63	1·70	1·10	0·40	5·7	7·47	4·2	2·0	1·7	2·1	0·38	0·32	1·4	0·38
La	La139	0·0090	0·003	0·53	0·27	4·5	2·52	0·62	0·05	12	8	0·53	0·25	1·4	0·28
Ce	Ce140	0·023	0·015	2·28	0·77	14·8	8·64	3·0	0·3	46	31	3·3	1·7	5·8	0·95
Pr	Pr141	0·0042	0·002	0·35	0·08	1·7	1·01	0·50	0·09	5·8	3·7	0·50	0·23	0·69	0·13
Nd	Nd143	0·019	0·004	1·72	0·35	5·8	3·07	2·4	0·6	23	14	2·8	1·1	2·64	0·51
Sm	Sm149	0·012	0·0001	0·64	0·06	1·2	0·34	0·80	0·29	5·4	2·5	1·0	0·34	0·60	0·04
Eu	Eu151	0·0069	0·001	0·13	0·02	0·26	0·06	0·15	0·03	0·97	0·38	0·24	0·07	0·12	0·01
Gd	Gd160	0·0080	0·001	0·86	0·12	1·22	0·06	0·84	0·34	5·9	0·7	1·1	0·34	0·49	0·08
Tb	Tb159	0·0020	0·0003	0·13	0·01	0·18	0·004	0·13	0·06	0·85	0·11	0·17	0·05	0·07	0·01
Dy	Dy163	0·020	0·007	0·84	0·12	1·20	0·11	0·92	0·44	5·1	0·8	1·4	0·36	0·47	0·07
Ho	Ho165	0·0060	0·003	0·16	0·03	0·26	0·02	0·18	0·09	0·95	0·30	0·29	0·07	0·10	0·01
Er	Er166	0·026	0·008	0·45	0·12	0·81	0·05	0·53	0·22	2·7	0·7	0·80	0·18	0·26	0·03
Yb	Yb172	0·118	0·027	0·46	0·19	0·96	0·04	0·55	0·25	3·1	0·4	1·2	0·25	0·35	0·07
Lu	Lu175	0·039	0·007	0·092	0·07	0·18	0·01	0·090	0·04	0·53	0·12	0·28	0·05	0·082	0·027
Hf	Hf179	0·332	0·133	0·19	0·07	0·16	0·01	0·18	0·06	1·2	0·7	0·34	0·07	0·21	0·09
Pb	Pb208	12·12	1·91	1·6	0·96	0·86	0·12	4·4	2·7	3·7	2·2	2·5	2·4	1·8	1·1
Th	Th232	0·0037	0·001	0·070	0·01	0·10	0·06	0·11	0·03	0·18	0·16	0·041	0·02	0·26	0·08
U	U238	0·353	0·151	0·044	0·02	0·10	0·08	0·083	0·031	0·14	0·13	0·076	0·04	0·20	0·01

n.a., not analyzed.

Table 3: Plagioclase compositions in the xenoliths

Major elements	MR	Plagioclase + Quartz + Pyroxene				Composite			
		L03-15				L03-4		L03-8	
		Av. type 1 $n=4$	SD type 1	Av. type 2	SD type 2	Av. $n=4$	SD	Av. $n=10$	SD
wt %									
SiO_2	Si28	51·58	1·09	58·15	0·94	54·77	0·68	53·22	2·70
Al_2O_3	Al27	30·98	1·60	26·47	0·55	28·69	0·88	29·83	2·04
FeO	Fe57	0·10	0·00	0·08	0·01	0·14	0·02	0·10	0·04
CaO	Ca43	13·50	0·65	8·26	1·31	10·87	0·85	12·17	1·38
Na_2O	Na23	3·78	0·04	6·67	1·63	4·90	0·31	4·42	1·47
K_2O	K39	0·16	0·05	0·43	0·15	0·73	0·05	0·36	0·09
P_2O_5	P31	0·016	0·016	0·01	0·00	0·003	0·001	0·008	0·004
Total		100		100		100		100	

Trace elements *ppm*	LR	Av. type 1 $n=3$	SD	type 2 $n=1$	Av. $n=4$	SD
Li	Li7	4·3	2·2	21	9·3	6·8
Mg	Mg25	325	198	341	335	105
Ti	Ti49	19	15	13	18	10
Cr	Cr53	2·7	0·7	3·0	1·6	1·0
Mn	Mn55	20	16	117	47	20
Cu	Cu63	23	4·9	7·5	7·4	3·5
Zn	Zn66	14	2	60	13	4
Rb	Rb85	11	9	4	3	1
Sr	Sr88	507	270	228	1349	594
Y	Y89	0·30	0·24	1·0	0·31	0·15
Zr	Zr91	0·15	0·09	0·14	0·97	1·83
Nb	Nb93	0·18	0·27	0·023	0·02	0·03
Cs	Cs133	0·09	0·075	0·11	0·001	0·003
Ba	Ba137	92	40	20	481	223
La	La139	0·87	0·26	5·4	1·00	0·45
Ce	Ce140	1·5	0·25	14	1·52	0·74
Pr	Pr141	0·12	0·03	1·2	0·12	0·05
Nd	Nd143	0·48	0·26	3·7	0·36	0·19
Sm	Sm149	0·07	0·03	0·49	0·053	0·02
Eu	Eu151	0·38	0·26	0·22	0·39	0·16
Gd	Gd160	0·11	0·12	0·34	0·027	0·013
Dy	Dy163	0·036	0·02	0·15	0·0089	0·003
Ho	Ho165	0·0064	0·004	0·025	0·0014	0·001
Er	Er166	0·087	0·13	0·079	0·0036	0·002
Yb	Yb172	0·031	0·03	0·053	0·0040	0·002
Lu	Lu175	0·0025	0·0008	0·0073	0·0007	0·0002
Hf	Hf179	0·017	n.a.	n.a.	0·070	0·092
Ta	Ta181	0·021	0·006	0·003	0·0083	0·009
Pb	Pb208	49	26	40	18	9
Th	Th232	0·40	0·68	0·071	0·01	0·02
U	U238	0·18	0·24	0·032	0·02	0·03

Table 4: Mica compositions (in wt %) in xenoliths

		Composite L03-8	
		Av. $n=2$	SD
SiO_2	Si28	39·96	1·98
TiO_2	Ti48, Ti49	1·59	0·31
Al_2O_3	Al27	17·84	1·37
FeO	Fe57	6·70	0·34
MgO	Mg25	27·94	0·07
MnO	Mn55	0·0875	0·0025
CaO	Ca43	1·03	0·49
Na_2O	Na23	0·25	0·01
K_2O	K39	4·49	0·43
P_2O_5	P31	0·0083	0·0029

Table 5: Quartz titanium contents

L03-15	Ti48	Ti49	Av. Ti	T (°C)*		
	(ppm)	(ppm)	(ppm)	$a_{Ti}=1$	$a_{Ti}=0·75$	$a_{Ti}=0·5$
9-L03-15-qtz-1	13	12	13	547	570	605
10-L03-15-qtz-2	8	11	9	525	546	579
11-L03-15-qtz-3	16	14	15	562	586	621
12-L03-15-qtz4	6	4	5	480	499	528
13-L03-15-qtz-5	9	9	9	519	540	572
14-L03-15-qtz-6	8	8	8	512	532	564
15-L03-15-qtz-7	10	9	10	528	549	582
16-L03-15-qtz-8	4	4	4	464	482	510
17-L03-15-qtz-9	7	6	7	501	521	552
18-L03-15-qtz-10	6	5	6	492	512	542
19-L03-15-qtz-11	10	9	9	525	547	580
20-L03-15-qtz-12	9	7	8	514	535	567
21-L03-15-qtz-13	6	5	6	492	512	542
22-L03-15-qtz-14	8	6	7	506	527	558
23-L03-15-qtz-15	7	7	7	506	527	558
124-L03-15-qtz-16	12	10	11	538	560	594
25-L03-15-qtz-17	10	8	9	519	540	573
26-L03-15-qtz-18	8	8	8	510	531	562
27-L03-15-qtz-19	9	8	9	519	540	572
28-L03-15-qtz-20	9	8	8	517	538	570
		Av.	8·3	514	535	567
		SD	2·6	22	23	25

*Estimated equilibration temperatures from Ti-in-quartz thermometry (Wark & Watson, 2006) assuming plausible range of TiO_2 activity.

pattern. In addition, the Lu contents of many of the pyroxenes are unusually enriched relative to the other REE, leading to a concave-upward pattern in the heavy REE (HREE). In particular, strong negative anomalies in Ba, Sr, and Eu indicate equilibrium with plagioclase. The pyroxenes also have unusually high Pb and Li contents. All pyroxenes have very low Ni (<30 ppm) and Cr (<5 ppm) abundances compared with typical magmatic clinopyroxenes in basalts, which generally have Ni and Cr contents exceeding 100 ppm (Table 2). Finally, we note that L03-3 pyroxenes (Fig. 7) differ from the above-described pyroxenes in that their REE abundances are ~100 times lower. In addition, L03-3 pyroxenes are LREE-depleted relative to the HREE and enriched in Ba, Sr, Eu, Pb, Cs and Rb relative to the REE. As we will show below, the relative abundance patterns in L03-3 pyroxenes are reminiscent of plagioclase abundance patterns.

Plagioclase

Plagioclase trace-element patterns are shown in Fig. 7b and the data are reported in Table 3. Plagioclase has low HREE contents compared with pyroxene, but its LREE abundances are similar to those of the coexisting pyroxene. The very low HREE abundances and relatively high LREE are manifested as strongly sloping LREE-enriched abundance patterns. As expected, all plagioclases show positive anomalies in Sr, Pb, Eu, and Ba. Cs contents are very low, but surprisingly, Rb/Sr ratios are much higher than that expected for plagioclase. Figure 7b also shows L03-3 pyroxene for comparison. It can be seen that the overall abundance pattern (e.g. spikes in Ba, Sr, and Eu) of the L03-3 pyroxene are very similar to that plagioclase.

Ti in quartz and thermometry

Titanium contents in quartz were determined only for sample L03-15, a composite xenolith (Table 5). The average of 18 grains yields Ti contents of $8·3 \pm 2·6$ ppm. Ti in quartz can be used as a thermometer (Wark & Watson, 2006) provided that the activity of TiO_2 in the rock is buffered or known. The presence of titanite in the plagioclase + quartz + pyroxene lithologies suggests a high TiO_2 activity (>0·6) (Ghent & Stout, 1984). We did not measure the composition of the titanite and hence cannot precisely define the TiO_2 activity beyond that bounded by the presence of titanite. Assuming a range of activities between 0·5 and 1 (conservative lower and upper bounds), we obtain temperature bounds between 510 and 570°C for the thermal conditions of last equilibration. Such temperatures are below the solidus temperatures of normal granites.

Reconstructed whole-rock compositions

Because of the heterogeneous nature of these xenoliths, we chose to reconstruct the whole-rock compositions from mineral modes and mineral chemistry rather than

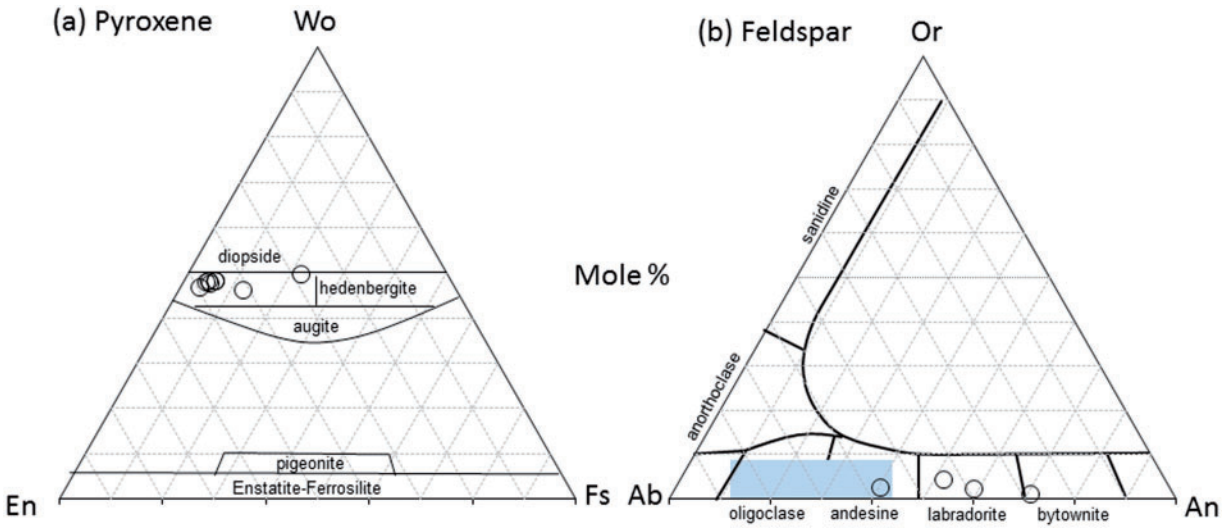

Fig. 6. (a) Pyroxene ternary diagram showing the compositions of the pyroxene in the xenoliths. (b) Feldspar ternary diagram showing composition of the plagioclase. Range of anorthite contents typical of granodiorites is shown. Wo, wollastonite; En, enstatite; Fs, ferrosillite; Or, orthoclase; Ab, albite; An, anorthite.

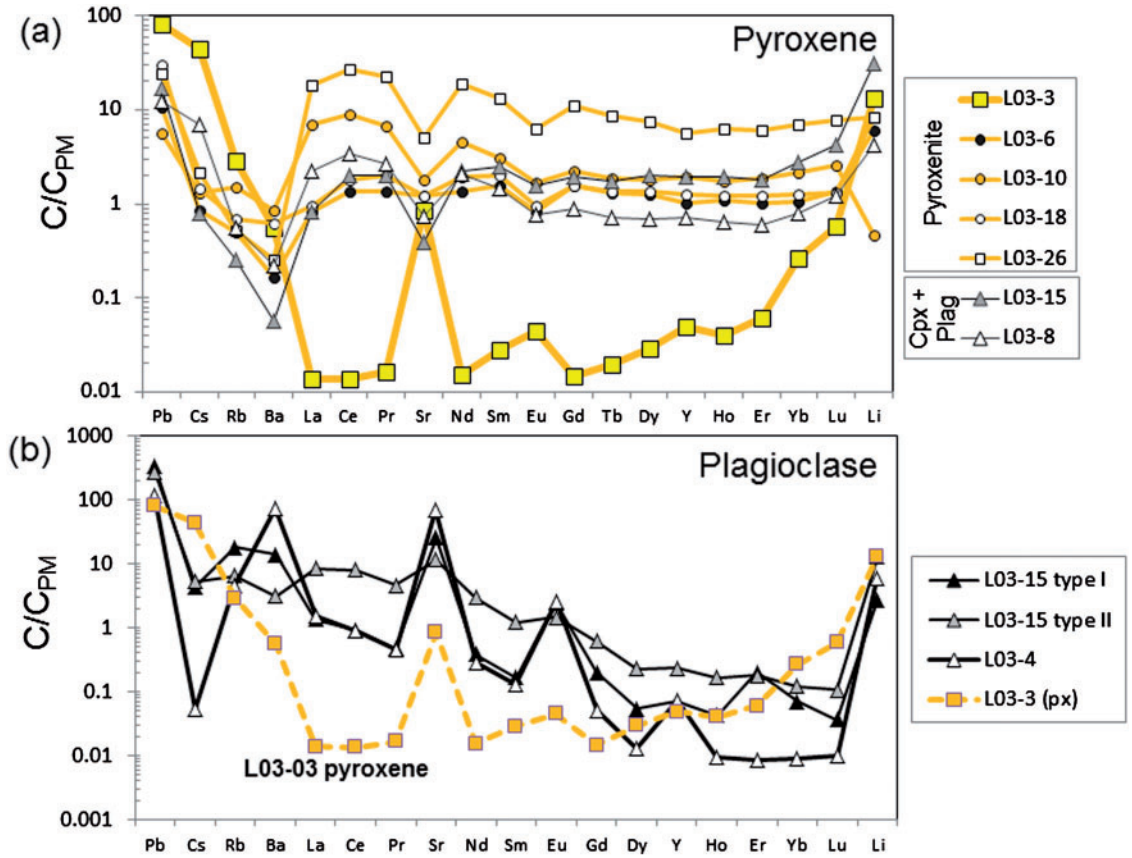

Fig. 7. (a) Primitive-mantle normalized trace element abundance patterns for pyroxenes, plotted in order of increasing compatibility in anhydrous basaltic systems. (b) Primitive-mantle normalized trace element abundance patterns for plagioclase. The unusual pyroxene from (a) (L03-3) with a 'ghost' plagioclase signature is plotted for comparison.

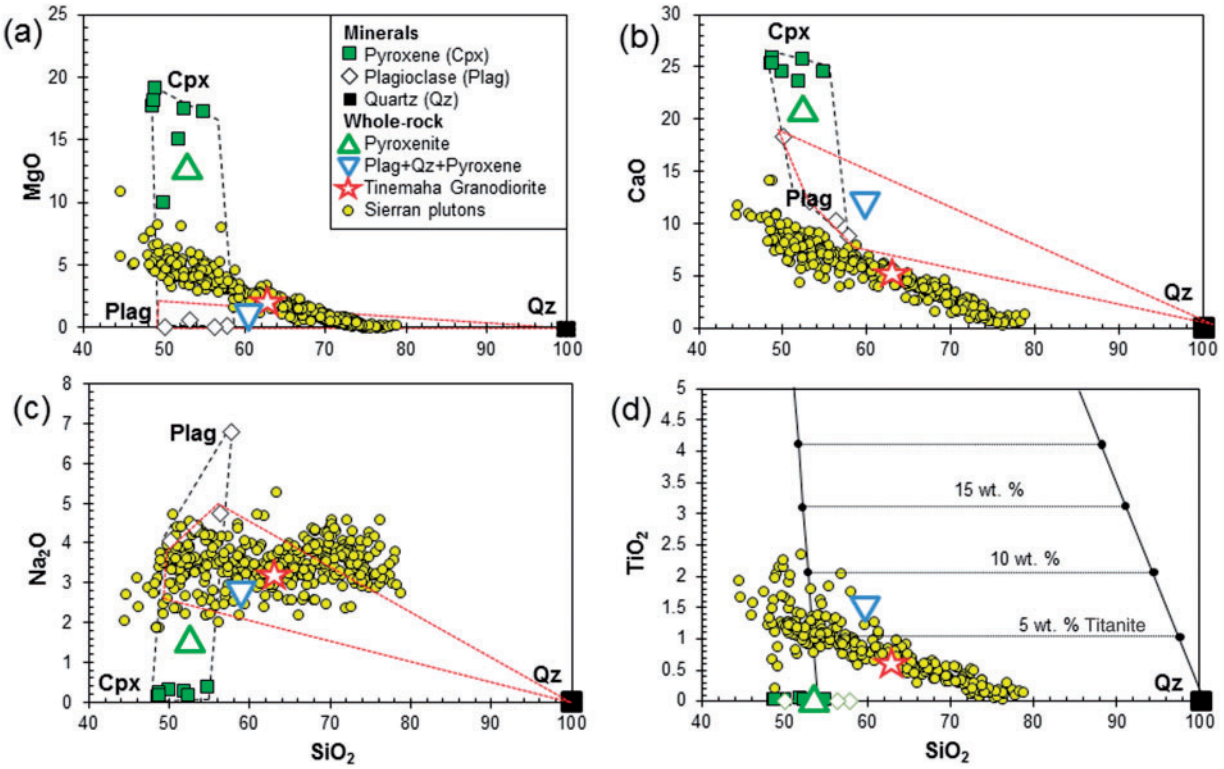

Fig. 8. (a–d) Permissible whole-rock major element compositions based on mixing arrays (bounded by dashed lines) between plagioclase, pyroxene, and quartz components. In (d), Ca-titanate is accounted for. Estimated whole-rock compositions reconstructed from mineral modes are shown by upward pointing triangles (pyroxenites) and downward pointing triangles (plagioclase + quartz ± pyroxene). Tinemaha granodiorite composition is denoted by a red star. Small circles represent Sierran plutonic rocks compiled from the literature (see text for data sources). In (d), mixing lines with a titanite component are shown. Dotted horizontal lines in (d) correspond to isopleths of constant titanite mode in increments of 5 wt %.

analyzing whole-rock powders. The advantage of using reconstructed compositions over whole-rock powders is that the natural variability in the bulk composition of these highly heterogeneous rocks can be assessed by treating the mineral proportions as variables within a specified range. In Fig. 8, we plot the compositions of single minerals: plagioclase, clinopyroxene, quartz, and titanite (the latter only for TiO_2). Mixing arrays connecting these mineral compositions then represent the range of permissible whole-rock compositions. Quartz does not occur in any of the pyroxenites and makes up only a small percentage (10–15%) of the quartz + plagioclase + pyroxene lithologies. For this reason, we have drawn binary mixing arrays between plagioclase and pyroxene and between quartz and plagioclase. Estimated whole-rock compositions are denoted within these mixing arrays. In Fig. 8d, we show the effect of titanite on whole-rock TiO_2 contents (titanite can be ignored in whole-rock reconstructions for the other major elements). We have assumed titanite to be stoichiometric $CaTiSiO_5$. Although small amounts of Al may exist in titanite, accounting for its presence would not significantly change the mass balance of TiO_2. Titanite was found only in the quartz-bearing lithologies and estimated at 5–10% by volume. Implied whole-rock TiO_2 contents are ~1–2 wt % (strictly speaking, a density correction to convert mineral modes to mass fraction is necessary, but this is not meaningful given the large uncertainties in the titanite mode owing to small-scale sample heterogeneity).

The abundance of titanite means that the estimated whole-rock TiO_2 (1–2 wt %) contents of the plagioclase + quartz + pyroxene lithologies are higher than that of the Tinemaha granodiorite (0·6 wt %). For comparison (Fig. 8), we also show the compositions of Sierran granitoid plutons compiled from the literature (Bateman, 1961; Ague & Brimhall, 1988*a*, 1988*b*; Bateman *et al.*, 1988; Barbarin *et al.*, 1989; Coleman & Glazner, 1997; Ratajeski *et al.*, 2001; Lee *et al.*, 2006, 2007). The average composition of the Tinemaha granodiorite (through which the Fish Springs cinder cone erupted) is denoted by a star in Fig. 8 (Bateman, 1961). Pyroxenites are characterized by 'basaltic' SiO_2 contents, but unusually high MgO and CaO and

low Na_2O and TiO_2 compared with the granitoid differentiation series. The plagioclase + quartz + pyroxene lithologies, in contrast, are richer in SiO_2 (~60 wt %) and also deviate from the granitoid differentiation series for certain elements (low MgO, high CaO).

DISCUSSION

The case for an endoskarn origin

We consider the following observations to be the most diagnostic.

(1) Some pyroxenites show textural and geochemical evidence for replacement of plagioclase by pyroxene as exemplified by the presence of optically continuous relict plagioclase grains crosscut or embayed by pyroxene and by 'ghost' trace-element signatures of plagioclase in pyroxenes (Figs 2 and 7).
(2) The pyroxenes are too diopsidic and too poor in Ni and Cr to have equilibrated with any reasonable mafic magma (Fig. 6 and Table 2).
(3) In the plagioclase + quartz ± pyroxene lithologies, the texture is predominantly equigranular; this overprints earlier igneous textures, leaving only a few igneous relicts (Fig. 3).
(4) Plagioclases in the plagioclase + quartz ± pyroxene lithologies are far richer in anorthite content (>50% An) than those (<40% An) typical of igneous rocks with quartz (granites and granodiorites) (Fig. 6b). There are also no alkali feldspars in these lithologies; however, the high quartz content suggests that the plutonic parental rock was granodioritic rather than dioritic.
(5) Except for phlogopite, there are no hydrous minerals in any of the lithologies studied. Moreover, phlogopite occurs exclusively at or near the contacts between pyroxenite and plagioclase + quartz lithologies (Figs 2b and 4b).
(6) There is local textural evidence for replacement of pyroxene by plagioclase at the contacts between felsic lithologies and pyroxenite (Fig. 2b).

The presence of relict igneous textures in the form of interlocking plagioclase crystals suggests that the felsic lithologies were originally plutonic rocks that subsequently underwent significant textural and compositional modification. However, the complete absence of alkali feldspars, the unusually high anorthite content of the plagioclase, and the lack of hydrous phases are all consistent with open-system behavior wherein certain chemical components were introduced or removed. Extensive evidence for near-complete to complete conversion of plagioclase to pyroxene (and vice versa) also attests to the importance of open-system mass exchange. Plagioclase cannot be converted to diopsidic pyroxene without adding Mg. Similarly, the reverse conversion—clinopyroxene to plagioclase—requires an external input of Al and removal of Mg and Fe. The concentration of phlogopite near the contact between pyroxenite and felsic lithologies further requires mass transfer of K and Al across this contact. The presence of primary fluid inclusions in plagioclase near to pyroxenite–felsite contacts attests to the pervasiveness of fluids in the formation of these lithologies.

We conclude from the petrographic and geochemical observations that these xenoliths probably had a granodiorite plutonic protolith. If so, significant inputs of Ca and Mg are required to generate clinopyroxene and Ca-rich plagioclase, and K and Na must have been largely removed. Additional insight into the composition of the Ca- and Mg-bearing fluids comes from the trace element abundances, particularly those of L03-3 pyroxenes, which carry a 'ghost' plagioclase signature in the form of a strong positive anomaly in Eu (Fig. 7). Because of the very strong preference of plagioclase for Eu compared with clinopyroxene, such a signature can be generated only by extensive conversion of plagioclase to pyroxene without significant addition of REE. This process is illustrated in Fig. 9, where we have calculated pyroxene REE compositions with progressive transformation of plagioclase into pyroxene (simulated by changing pyroxene/plagioclase ratio) in a system closed to the REE. In these calculations, the REE were redistributed with changing pyroxene/plagioclase mode according to estimated REE partition coefficients between pyroxene and plagioclase (for internal consistency, these partition ceofficients were calculated from the measured ratios of REE in pyroxene to plagioclase in the pyroxenite lithologies themselves). Because REE (with the exception of Eu) are more compatible in clinopyroxene than in plagioclase, any addition of a REE-bearing fluid would have erased the ghost plagioclase signature in the clinopyroxenes. For these reasons, we conclude that the fluids responsible for metasomatizing the granodioritic pluton were Ca- and Mg-rich, but REE-poor. Carbonate-derived fluids seem to fit these requirements. Given the close proximity of the Fish Springs cinder cone to the Poverty Hills marble complex and other Paleozoic limestones and dolomites in the region (Fig. 1), this hypothesis is also geologically reasonable. We thus speculate that the xenoliths in this study represent fragments of the metasomatized margins of a granodiorite pluton generated by heat and mass exchange between the pluton and wall-rocks of Paleozoic carbonate.

Assuming that the Ti-in-quartz temperatures of 510–570°C represent equilibrium conditions just prior to entrainment of the xenoliths into the Fish Springs volcano, we can estimate the approximate depth from which these xenoliths were derived if the surface heat flux is known and a steady-state geotherm is assumed. Taking a measured surface heat flux in the Sierra Nevada of

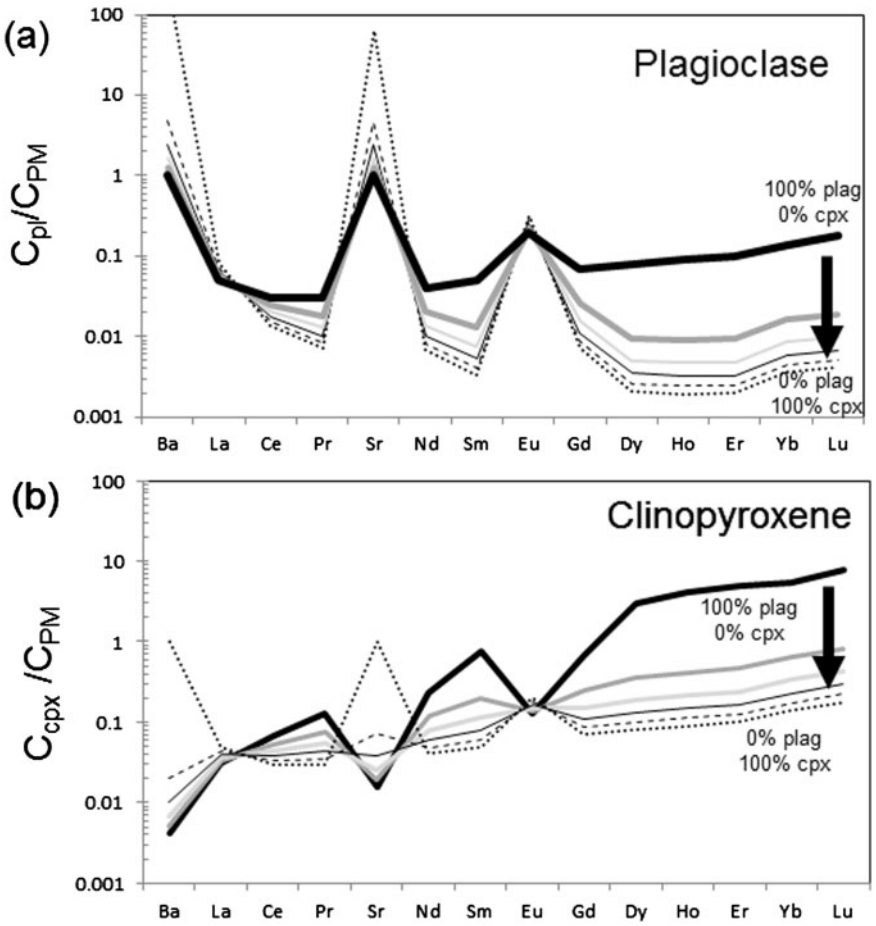

Fig. 9. (a, b) Results of model to show how a clinopyroxene might inherit a 'ghost' plagioclase trace element signature by metasomatic replacement of plagioclase by pyroxene. The model begins with a system containing 100% plagioclase, with a trace-element signature indicated by the bold black line in (a) and (b). The model assumes the system remains closed to rare earth elements, Ba, and Sr, but open to Ca and Mg so that plagioclase can be converted to clinopyroxene. Trace elements are assumed to be distributed according to equilibrium partitioning, using partition coefficients based on observed ratios of these elements between pyroxene and plagioclase in the pyroxenite lithologies in this study. Different lines represent predicted plagioclase and pyroxene trace element signatures with progressive conversion of plagioclase to pyroxene in 20% increments. Pyroxenes inherit a positive Eu anomaly when >70% plagioclase is converted.

$\sim$40 mW m^{-2} (Lachenbruch, 1968) and assuming a thermal conductivity of $\sim$2·5 W m^{-1} K^{-1} yields a depth of $\sim$15 km. However, a higher surface heat flux is probably more appropriate given that the Fish Springs cinder cone lies in the volcanically active Owens Valley graben. If we use a surface heat flux of 80 mW m^{-2} (Henyey & Lee, 1976), the depth of origin is $\sim$7 km, suggesting a mid-crustal origin. These calculations come with considerable uncertainties. For example, depths could be under- or overestimated if the geotherm is not at steady state. Also, accounting for crustal heat production would increase the depth estimates. If, however, the Ti-in-quartz temperatures represent closure temperatures frozen in during emplacement and cooling of the magma body into the crust, then the above temperature estimates are not relevant to present-day geotherms and the depth estimates are maximum bounds.

Conceptual model for endoskarn formation

The intrusion of a granodioritic pluton into carbonate wall-rocks will result in strong chemical potential gradients across the contact, driving mass exchange. Mass transfer between the pluton and the carbonate can be visualized in Fig. 10, in which we have plotted possible reactions in a Al_2O_3–SiO_2–CaO–(MgO,FeO) pseudo-quaternary diagram, modified from Kerrick (1977). In this diagram, pluton-related fluids will be rich in SiO_2 (pluton fluid denoted by the star) whereas carbonate-derived fluids will be enriched in CaO and MgO. The lines connecting the granodioritic fluid to the carbonate fluids transect the entire volume of the tetrahedron. Within the pluton itself (low Ca and Mg), fluids will be in equilibrium with plagioclase, quartz and a hydrous mafic phase, such as hornblende or biotite. If the CaO and MgO activity in the fluid increases, the diopside–plagioclase–quartz

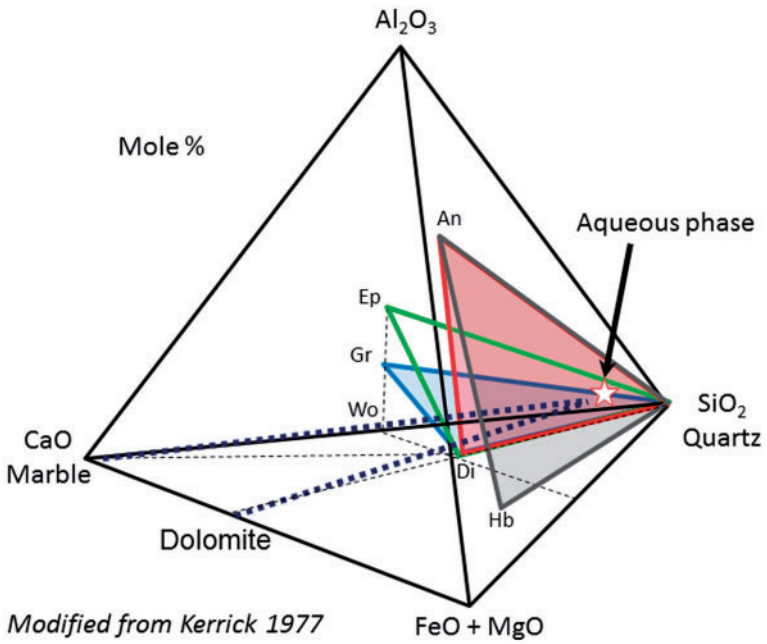

Fig. 10. Pseudo-quaternary diagram showing the types of reactions that could occur along a compositional gradient in a fluid. Fluids in equilibrium with granodioritic magma are denoted by the star. Those in equilibrium with carbonate-rich rocks fall towards the carbonate endmember join. Bold dotted lines correspond to possible compositional variations in the fluid composition if the fluids were simply mixtures between the two endmember compositions. Intersection of these fluid 'lines' with the shaded triangles, whose apices are defined by various mineral phases, dictates how the mineralogy changes with fluid composition. Diagram is redrawn from Kerrick (1977). Ep, epidote; Gr, grossular; Wo, wollastonite; Di, diopside; Hb, hornblende; An, anorthite.

'ternary' is intersected, resulting in the conversion of hornblende or biotite into diopside. These lithologies would be considered 'endoskarns' if their protolith is the pluton. Further addition of Ca and Mg, however, results in the formation of typical skarn minerals (epidote, grossluar, wollastonite, etc.) within the marble itself. These are called exoskarns because their protoliths are the surrounding country-rock.

In Fig. 11a, we schematically show how spatial variations in chemical potential will drive mass transfer of specific elements. The carbonate country-rock is on the left and the pluton is on the right. Components such as SiO_2, Al_2O_3, Na_2O, K_2O and H_2O are high in the granodiorite and low in the carbonates; hence, these components will tend to migrate towards the carbonates via hydrothermal water-rich fluids emanating from the pluton itself. In contrast, components such as CaO, MgO and CO_2 are higher in the carbonates and therefore will migrate into the granodiorite (Satish-Kumar *et al.*, 2004). By 'migrate', we envisage a diffusional process either in the solid state or through an interconnected network of fluids, the latter being more likely and effective because diffusivities in fluids are orders of magnitude faster than in solids. Magma–wall-rock contacts are probably bathed in hydrothermal fluids derived from the pluton or from pore waters and decarbonation reactions in the carbonate wall-rock. If chemical potential gradients are sufficiently high and in the appropriate direction, diffusion via fluids could go against the direction of overall advective circulation. Evidence for such metasomatic behavior is seen in many contact metamorphic aureoles (e.g. Woodford *et al.*, 2001).

To explain the spatial zonations in mineralogy, we envision the following scenario. The pyroxenite lithologies most probably represent the contact between the pluton and the marble, separating exoskarn from endoskarn. Diopsidic clinopyroxene is generated by reaction of Si with dolomite, liberating CO_2:

$$2SiO_2 + CaMg(CO_3)_2 \rightarrow CaMgSi_2O6 + 2CO_2 \uparrow . \quad (1a)$$

If pure limestone is involved, the equivalent decarbonation reaction is

$$SiO_2 + CaCO_3 \rightarrow CaSiO_3 + CO_2 \uparrow \quad (1b)$$

and wollastonite is formed. The decarbonation in reaction (1) generates CO_2 in the country-rock, which should impart a strong gradient in the activity of CO_2 that drives CO_2 into the pluton (Figs 10 and 11). Influx of CO_2 into the pluton would dilute the activity of H_2O, which could then destabilize hydrous minerals in the granodiorite.

The high Ca and Mg content of the carbonates and the clinopyroxenes would generate a strong Ca and Mg

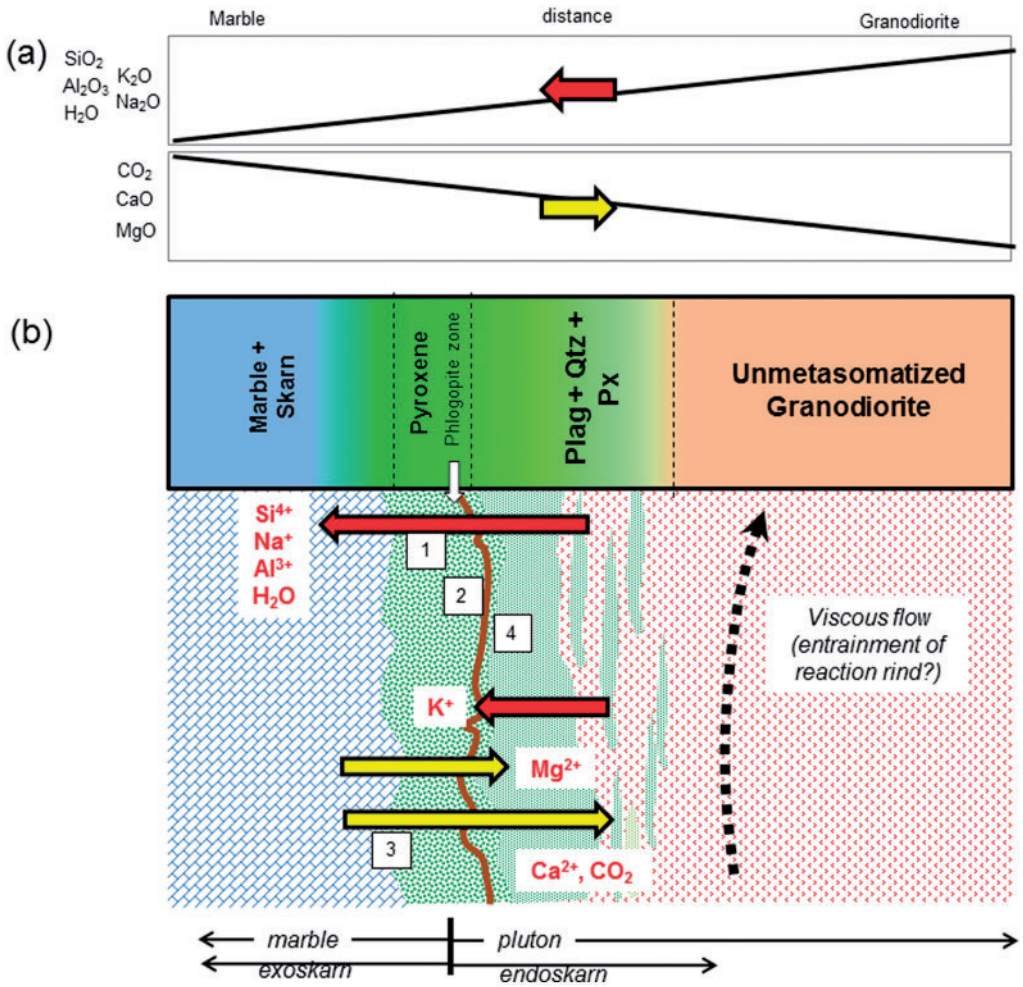

Fig. 11. (a) Schematic diagram showing how chemical gradients will drive diffusive transport. *y*-axis represents qualitative chemical potential; *x*-axis represents qualitative distance between carbonate wallrock (left) and pluton (right). Arrows show the direction in which each of these elements will flow. (b) Geological reconstruction of endoskarn and exoskarn formation in the context of the xenoliths investigated in this study. Pyroxenites define the contact between the marble country rock and the pluton. Plagioclase + quartz + pyroxene lithologies define the outer envelope (endoskarn) of the pluton that has been metasomatized by fluids from the country rock. Arrows denote the direction of element transport. The extent to which the arrows extend into the pluton or carbonate wall-rock indicates qualitatively the relative extent to which these elements might migrate. Numbers refer to reactions in the text.

chemical potential gradient directed into the pluton. Migration of Mg into the pluton could result in the conversion of plagioclase to clinopyroxene:

$$MgO + CaAl_2Si_2O_8 \rightarrow CaMgSi_2O_6 + Al_2O_3 \quad (2)$$

Here, we have assumed that the metal oxides MgO and Al_2O_3 represent species in the melt or fluid. We speculate that reaction (1) dominates at the contact, but reaction (2) dominates just within the margins of the pluton. Pyroxenites with ghost plagioclase trace-element signatures may have formed via reaction (2). As reaction (2) proceeds, Mg should eventually be consumed, limiting the extent to which clinopyroxene formation can extend into the pluton. Reaction (2) also liberates Al, which may have important local effects. Al will tend to 'flow' in the direction of the carbonates and clinopyroxene, which could result in local reversal of reaction (2) and allow for replacement of clinopyroxene by plagioclase.

Ca, on the other hand, is not affected directly by reaction (2) and hence diffusional transport of Ca ions could progress much farther into the pluton than Mg. Ca influx into the pluton would convert albite and orthoclase components to anorthite via the following reactions:

$$CaO + 2NaAlSi_3O_8 \rightarrow CaAl_2Si_2O_8 + Na_2O + 4SiO_2 \quad (3a)$$

$$CaO + 2KAlSi_3O_8 \rightarrow CaAl_2Si_2O_8 + K_2O + 4SiO_2. \quad (3b)$$

Such reactions can account for the absence of alkali feldspar in our studied samples and for the unusually

anorthitic content of the plagioclase. The release of Si by reactions (3a) and (3b) should enhance the formation of quartz. In addition, subsequent migration of Si into the carbonate will probably generate clinopyroxene by decarbonation via reaction (1). Na and K ions will also tend to migrate towards the carbonate. There is no obvious sink for Na in the endoskarn lithologies as the diopsidic clinopyroxenes are not able to accommodate significant amounts of Na. Na will thus be transported into the exoskarn region, possibly forming scapolite or other Na-bearing minerals. As for K, its migration from the pluton towards the carbonate wall-rock appears to have generated phlogopite. Generation of phlogopite, however, also requires Mg and Al. Indeed, the observed localization of phlogopite at the contacts between pyroxenite and felsic lithologies (Figs 2b and 4b) suggests that the source of the Mg is clinopyroxene. This suggests the following reaction, which converts clinopyroxene into phlogopite:

$$K_2O + Al_2O_3 + 2H_2O + 6CaMgSi_2O_6 \rightarrow 2KMg_3AlSi_3O_{10}(OH)_2 + 6CaO + 6SiO_2. \quad (4)$$

The source of the Al is probably reaction (2), which means that if we combine reactions (2) and (4), we arrive at another reaction:

$$K_2O + MgO + 2H_2O + CaAl_2Si_2O_8 + 5CaMgSi_2O_6 \rightarrow 2KMg_3AlSi_3O_{10}(OH)_2 + 6CaO + 6SiO_2. \quad (5)$$

Reaction (5) shows that phlogopite (Phl) formation occurs when K-rich fluids react with plagioclase and clinopyroxene in the presence of excess dissolved Mg. This explains why phlogopite occurrence is restricted to the contacts between the pyroxenite and the felsic lithologies.

The above effects of open-system behavior on the mineral assemblages are graphically illustrated in Fig. 12 using activity–activity diagrams (e.g. van Marcke de Lummen & Verkaeren, 1986). Stability fields of plagioclase (An), clinopyroxene (Di) and phlogopite (Phl) are shown as a function of oxide activities (the above equations were used to construct these diagrams; further details are given in the figure caption). For example, in Fig. 12a, high Al_2O_3 activity favors plagioclase and high MgO activity favors clinopyroxene. In Fig. 12b, high Al_2O_3 and K_2O activities favor phlogopite over clinopyroxene. Increasing H_2O activity expands the phlogopite stability field, but increasing CaO and SiO_2 activity decreases the phlogopite stability field with respect to clinopyroxene. In Fig. 12c, the relationships between three mineral phases are shown on a K_2O vs MgO activity diagram for two Al_2O_3 activities. In this set of diagrams, it can be seen that increasing Al_2O_3 activity increases both the plagioclase and phlogopite stability fields relative to clinopyroxene. These diagrams can be used to assess how the mineralogy changes with changes in bulk composition along a compositional gradient from the pluton into the wall-rock. To illustrate, the wall-rock contact would be characterized by a pyroxenite zone corresponding to state 1 in Fig. 12. This state is represented by Al_2O_3 activities too low to stabilize plagioclase and phlogopite, hence pyroxene is the only stable phase. To stabilize phlogopite, elevated K_2O and Al_2O_3 activities are needed. For a constant K_2O activity, as shown in Fig. 12c, phlogopite appears when the Al_2O_3 or MgO activities increase (Fig. 12c, right-hand panel), thus explaining why phlogopite preferentially occurs within the contact zone between the pyroxenite and the felsic lithologies characterizing the pluton body.

Implications for net mass transport between pluton and country-rock

Large mass changes are implied by the above reactions, underscoring the open-system behavior of endoskarn formation. To evaluate the net magnitude and sign of mass exchange during the formation of these endoskarns, we consider the stoichiometry of the above reactions. The intrusion of a granodioritic pluton into carbonates will result in strong chemical gradients across the contact, driving mass exchange. Assuming that aqueous and volatile species leave the system, conversion of dolomite to pyroxene [reaction (1)] results in an ~17% increase in mass because Si is incorporated into pyroxene and CO_2 is lost. All other reactions as written above impart a decrease in mass. Conversion of plagioclase to pyroxene [reaction (2)] results in an ~17% decrease in mass, the missing mass representing Al species. Replacement of the albite and orthoclase component in feldspar with anorthite [reaction (3)] results in ~50% relative mass decrease because 2 moles of albite (or orthoclase) are converted for every 1 mole of anorthite generated. The missing mass is associated with loss of Na and Si, both of which will flow towards the carbonate, with the latter promoting formation of clinopyroxene or wollastonite and the release of CO_2. The generation of phlogopite results in an ~40% decrease in mass, liberating Ca and Si into the aqueous fluids, the former migrating towards the pluton and the latter towards the carbonates.

The net mass change associated with the metasomatism of the granodiorite can also be assessed by considering the initial elemental abundances in the plutonic protolith. For example, the total amount of K in the granodiorite protolith is small, so mass losses associated with phlogopite formation are probably of second order. However, the alkali feldspar mode in granodiorites may be as high as ~20–30 wt %. If all alkali feldspars were converted to plagioclase by reaction (3), we would expect a substantial mass loss from the pluton. For every 100 g of granodiorite, endoskarn formation results in a net mass loss of at least 10–15 g from the magma. Thus, even though the outermost

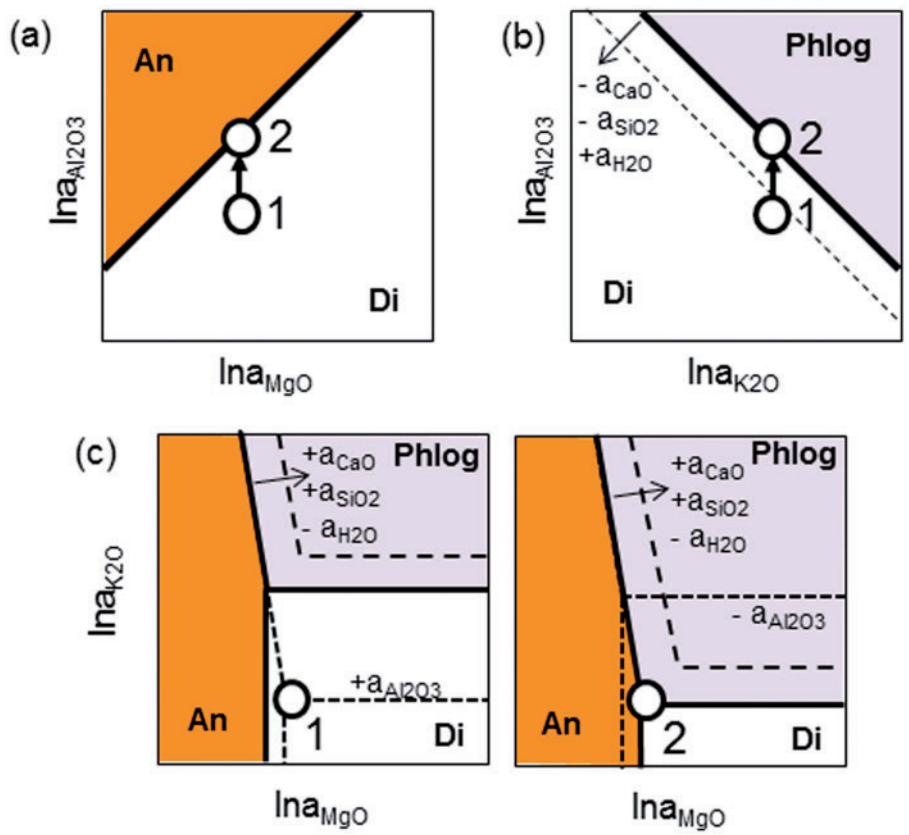

Fig. 12. Schematic activity–activity diagrams showing the stability fields of different mineral assemblages depending on the bulk composition of the system. (a) Al_2O_3 activity vs MgO activity. (b) Al_2O_3 activity vs K_2O activity for a given CaO, SiO_2 and H_2O activity. (c) K_2O activity vs MgO activity for a given CaO, SiO_2 and H_2O activity. In (a), the bold black line defines the coexistence of plagioclase (An) and clinopyroxene (Di) representing the reaction $MgO + CaAl_2Si_2O_8 = CaMgSi_2O_6 + Al_2O_3$. In (b), the bold black line defines the coexistence of clinopyroxene (Di) and phlogopite (Phl) based on the reaction $K_2O + Al_2O_3 + 2H_2O + 6CaMgSi_2O_6 = 2KMg_3AlSi_3O_{10}(OH)_2 + 6CaO + 6SiO_2$ (CaO, H_2O and SiO_2 activity held constant). Dashed contour shows how the reaction curve translates when a_{H2O} increases (expands Phl field) and a_{CaO} and a_{SiO2} decrease (decreases Di field). (c). Phase stability diagrams at constant Al_2O_3 activities. Bold black lines represent the coexistence of two mineral phases. The Phlog–An line represents the reaction $K_2O + 3CaAl_2Si_2O_8 + 6MgO + 2H_2O = 2KMg_3AlSi_3O_{10}(OH)_2 + 3CaO + 2Al_2O_3$. The An–Di reaction represents the same reaction as in (a) at a given a_{Al2O3}. The Phlog–Di line represents same reaction as in (b) at a given a_{Al2O3}. The triple point represents the coexistence of all three phases representing the reaction $MgO + K_2O + 2H_2O + CaAl_2Si_2O_8 + 5CaMgSi_2O_6 = 2KMg_3AlSi_3O_{10}(OH)_2 + 6CaO + 6SiO_2$. Al_2O_3 activity increases from (a) to (b), increasing the stability fields of plagioclase and phlogopite. Long-dashed lines show the effect of increasing CaO and SiO_2 activities and decreasing H_2O activity. Short-dashed line in (b) shows the effect of decreasing a_{Al2O3}. Circles labeled 1 and 2 represent two bulk compositions wherein a_{Al2O3} increases from state 1 to state 2 but a_{K2O} and a_{MgO} remain constant. In state 1, the system is too depleted in K and Al to stabilize phlogopite and plagioclase, and therefore is situated in the clinopyroxene stability field in all three diagrams. State 2 is characterized by an increase in a_{Al2O3}, resulting in the reaction of clinopyroxene to plagioclase and the reaction of both of these phases with K to generate phlogopite. It should be noted that for a given constant K content in a system, such as would be the case if K_2O activity was controlled by a pervasive hydrothermal fluid, phlogopite first becomes stable at the contact zone between plagioclase and clinopyroxene.

envelope of the magma experiences a net gain of Mg and Ca derived from the carbonates, there is net transfer of Na, K, Si and Al from the pluton to the country-rock.

These predicted mass losses may also explain the anomalously high titanite content and whole-rock TiO_2 of the reconstructed plagioclase + quartz + pyroxene lithologies (Fig. 8d). Owing to its generally low solubility in aqueous fluids compared with most other elements, it is commonly assumed that Ti is a relatively immobile element in metamorphic systems. Thus, total mass loss can be estimated from the extent to which TiO_2 has increased (Ague, 1994, 2003). The relative mass loss can be expressed as

$$1 - \frac{M_{\mathrm{rock}}}{M_{\mathrm{o}}} = 1 - \frac{C_{\mathrm{o}}}{C_{\mathrm{rock}}} \qquad (6)$$

where M_{rock} is the mass of the metasomatized rock, M_{o} is the mass of the protolith, C_{o} is the concentration of an immobile element in the protolith, and C_{rock} is the concentration in the metasomatized rock. Assuming C_{o} for TiO_2 to be that of the Tinemaha granodiorite (0·6 wt %) and

C_{rock} to be ~1·5 wt % yields an apparent mass loss of 60%. We note, however, that this result has considerable uncertainty because the estimated whole-rock TiO_2 contents depend on our calculated titanite modes, which are poorly constrained owing to 'nugget' effects. Also, Ti may not be perfectly immobile. Despite these uncertainties, the enhanced titanite modes in the plagioclase + quartz + pyroxene lithologies require significant mass losses, which must have been transferred into the surrounding carbonate rocks to generate skarns.

Insights into reactive wall-rock assimilation

A limitation of xenolith studies is that large-scale spatial relationships are not easily assessed. However, the abundance of endoskarn xenoliths in the Fish Springs cinder cone leads us to speculate that they may be extensive. This is in contrast to studies of contact metamorphic zones in the Sierran roof pendants, which show endoskarn formation on only small length scales (<1 m; Kerrick, 1970, 1977). If the temperatures recorded by Ti-in-quartz thermometry reflect metamorphic equilibration at mid-crustal depths, then relatively slow cooling rates would be expected to favor extensive endoskarn formation (but as noted above, it is also possible that the recorded temperatures were frozen in during cooling of the pluton).

Some important implications follow if these endoskarns are spatially extensive. They represent an inner metasomatic aureole of the pluton that effectively buffers the pluton from direct assimilation of wall-rocks. The foliated fabrics in the innermost plagioclase + quartz + clinopyroxene lithologies suggest that they were sheared by magmatic flow in the pluton itself. The dominance of subsolidus metamorphic textures (equigranular) suggests that they were deformed in the solid state; Ti-in-quartz thermometry indicates that temperatures were high enough to permit ductile flow. Thus, the innermost endoskarns are possible candidates for physical assimilation into the pluton itself, and because they are the products of metasomatic reaction, their compositions do not match exactly that of the wall-rock. Assimilation of these reacted products will generate 'mixing' trends in plutons that deviate from conventional linear mixing lines between wall-rock and magma. For example, Fig. 8 contrasts the effects of endoskarn assimilation with the overall compositional range for Sierran plutonic rocks. Based on the prediction of these distinctive trends, it appears that Sierran plutons as a whole have not experienced significant assimilation of carbonate rocks, but it does not rule out the possibility of extensive reaction on the margins of the plutons. Given the common occurrence of carbonate roof pendants in the eastern Sierras (Lackey & Valley, 2004), more detailed studies of pluton margins are needed to quantify the spatial extent of endoskarn and skarn formation during the emplacement of the Sierra Nevada batholith.

A key by-product of the metasomatic reactions between carbonate and silicic magmas is that CO_2 is generated when silicic magmas react with carbonates via decarbonation reactions [equation (1)]. Release of CO_2 will decrease the H_2O activity of magmatic fluids, and because CO_2 has a much lower solubility than H_2O in silicate liquids, particularly at low pressures (Newman & Lowenstern, 2002; Liu *et al.*, 2005), the granite solidus will be raised. Interaction with carbonate rocks at shallow pressures may thus cause the outer margins of a pluton to crystallize, limiting the extent to which plutons can directly 'assimilate' carbonate. However, at higher pressures and temperatures, such as in the mid-crust, CO_2 solubility in magmas could be sufficient to depress the solidus, which would favor extensive endoskarn formation. Our study adds to the growing evidence that reactive assimilation of carbonates may play a role in magmatic differentiation (Fulignati *et al.*, 2000, 2004; Barnes *et al.*, 2003, 2005; Deegan *et al.*, 2010).

CONCLUSIONS

Crustal xenoliths from the Quaternary Fish Springs cinder cone in the Big Pine volcanic field (California) represent fragments of endoskarns formed by the metasomatic reaction of granodiorite magmas with Paleozoic carbonates (dolomite) at mid-crustal depths. This conclusion is based on the presence of relict plutonic textures and mineralogies, extensive evidence for metasomatic replacement of igneous plagioclase by pyroxene, and replacement of alkali (K, Na) feldspar components by anorthite. Diopside-rich pyroxenites represent the products of carbonate–silica decarbonation reactions at the contact between the pluton and the wall-rock marble. Release of potassium during these metasomatic reactions generated a net flux of K from the pluton towards the carbonate country-rock, resulting in the precipitation of phlogopite within the pyroxenites. Theory- and observation-based mass-balance calculations implicate a net loss of mass from the pluton margins towards the marbles. Most of this mass loss was associated with losses of Na, K, and Si, but the pluton margins (endoskarn) appear to have gained Ca and Mg. These mass exchanges must have been accompanied by large losses of CO_2 from the country-rock.

ACKNOWLEDGEMENTS

This work represents Dyer's undergraduate research project. All of the data reported here were collected and analyzed by Dyer. We thank Terry Plank, Don Forsyth, and Ashley Tibbets for help and camaraderie in the field. Jade Star Lackey, Sarah Penniston-Dorley, Calvin Barnes and Kenneth Johnson are thanked for their reviews. We also thank Ron Frost for his comments and suggestions.

FUNDING

Field work was initially supported by Rice University's endowment for class field trips and in part by an Earthscope NSF (EAR 0745540) grant to Lee. Leeman acknowledges NSF support for time spent working on this project.

REFERENCES

Ague, J. J. (1994). Mass transfer during Barrovian metamorphism of pelites, south–central Connecticut, I: Evidence for composition and volume change. *American Journal of Science* **294**, 989–1057.

Ague, J. J. (2003). Fluid infiltration and transport of major, minor, and trace elements during regional metamorphism of carbonate rocks, Wepawaug Schist, Connecticut, USA. *American Journal of Science* **303**, 753–816.

Ague, J. J. & Brimhall, G. H. (1988*a*). Magmatic arc asymmetry and distribution of anomalous plutonic belts in the batholiths of California: effects of assimilation, crustal thickness and depth of crystallization. *Geological Society of America Bulletin* **100**, 912–927.

Ague, J. J. & Brimhall, G. H. (1988*b*). Regional variations in bulk chemistry, mineralogy, and the compositions of mafic and accessory minerals in the batholiths of California. *Geological Society of America Bulletin* **100**, 891–911.

Barbarin, B., Dodge, F. C. W., Kistler, R. W. & Bateman, P. C. (1989). Mafic inclusions, aggregates and dikes in granitoid rocks, central Sierra Nevada batholith, California—analytic data. *US Geological Survey Bulletin* **1899**, 1–28.

Barnes, C. G., Prestvik, T., Barnes, M. A. W., Anthony, E. Y. & Allen, C. M. (2003). Geology of a magma transfer zone: the Hortavaer igneous complex, north–central Norway. *Norwegian Journal of Geology* **83**, 187–208.

Barnes, C. G., Prestvik, T., Sundvoll, B. & Surratt, D. (2005). Pervasive assimilation of carbonate and silicate rocks in the Hortavaer igneous complex, north–central Norway. *Lithos* **80**, 179–199.

Bateman, P. C. (1961). Granitic formations in the east–central Sierra Nevada near Bishop, California. *Geological Society of America Bulletin* **72**, 1521–1537.

Bateman, P. C., Clark, L. D. *et al.* (1963). The Sierra Nevada batholith: a synthesis of recent work across the central part. *U.S. Geological Survey Professional Paper* **414-D**, 1–46.

Bateman, P. C., Chappell, B. W., Kistler, R. W., Peck, D. L. & Busacca, A. (1988). Tuolumne Meadows quadrangle, California–analytic data. *US Geological Survey Bulletin* **33**, 1–33.

Beard, B. L. & Glazner, A. F. (1995). Trace element and Sr and Nd isotopic composition of mantle xenoliths from the Big Pine volcanic field, California. *Journal of Geophysical Research* **100**, 4169–4179.

Bierman, P. R., Gillespie, A. R., Whipple, K. & Clark, D. (1991). Quaternary geomorphology and geochronology of Owens Valley, California. In: Walawender, M. J. & Hanan, B. B. (eds) *Geological Excursions in Southern California: Guidebook for the 1991 Annual Meeting.* San Diego, CA: Geological Society of America, pp. 199–223.

Blondes, M. S., Reiners, P. W., Ducea, M. N., Singer, B. & Chesley, J. T. (2008). Temporal–compositional trends over short and long time-scales in basalts of the Big Pine Volcanic Field, California. *Earth and Planetary Science Letters* **269**, 140–154.

Bohrson, W. A. & Spera, F. J. (2001). Energy-constrained open-system magmatic processes II: application of energy-constrained assimilation fractional crystallization (EC-AFC) model to magmatic systems. *Journal of Petrology* **42**, 1019–1041.

Brock, K. J. (1972). Genesis of Garnet Hill Skarn, Calaveras County, California. *Geological Society of America Bulletin* **83**, 3391–3404.

Coleman, D. R. & Glazner, A. F. (1997). The Sierra crest magmatic event: rapid formation of juvenile crust during the Late Cretaceous in California. *International Geological Review* **39**, 768–787.

Deegan, F. M., Troll, V. R., Freda, C., Misiti, V., Chadwick, J. P., McLeod, C. L. & Davidson, J. P. (2010). Magma–carbonate interaction processes and associated CO_2 release at Merapi volcano, Indonesia: insights from experimental petrology. *Journal of Petrology* **51**, 1027–1051.

DePaolo, D. J. (1981). Trace element and isotopic effect of combined wall-rock assimilation and fractional crystallization. *Earth and Planetary Science Letters* **53**, 189–202.

DePaolo, D. J., Perry, F. V. & Baldridge, W. S. (1992). Crustal versus mantle sources of granitic magmas: a 2-parameter model based on Nd isotopic studies. *Transactions of the Royal Society of Edinburgh, Earth Sciences* **83**, 439–446.

Ducea, M. N. & Saleeby, J. B. (1996). Buoyancy sources for a large, unrooted mountain range, the Sierra Nevada, California: evidence from xenolith thermobarometry. *Journal of Geophysical Research* **101**, 8229–8244.

Ernst, W. G. (1976). *Petrologic Phase Equilibria.* San Francisco, CA: W. H. Freeman.

Fulignati, P., Marianelli, P., Santacroce, R. & Sbrana, A. (2000). The skarn shell of the 1944 Vesuvius magma chamber. Genesis and P–T–X conditions from melt and fluid inclusion data. *European Journal of Mineralogy* **12**, 1025–1039.

Fulignati, P., Marianelli, P., Santacroce, R. & Sbrana, A. (2004). Probing the Vesuvius magma chamber–host rock interface through xenoliths. *Geological Magazine* **141**, 417–428.

Gans, W. T. (1974). Correlation and redefinition of the Goodsprings dolomite, southern Nevada and eastern California. *Geological Society of America Bulletin* **85**, 189–200.

Gao, S., Liu, X., Yuan, H., Hattendorf, B., Günther, D., Chen, L. & Hu, S. (2002). Determination of forty two major and trace elements in USGS and NIST SRM glasses by laser ablation-inductively coupled plasma-mass spectrometery. *Geostandards News* **26**, 181–196.

Ghent, E. D. & Stout, M. Z. (1984). TiO_2 activity in metamorphosed pelitic and basic rocks: principles and applications to metamorphism in southeastern Canadian Cordillera. *Contributions to Mineralogy and Petrology* **86**, 248–255.

Greene, D. C. & Stevens, C. H. (2002). Geologic map of Paleozoic rocks in the Mount Morrison Pendant, Eastern Sierra Nevada. California: California Department of Conservation, Division of Mines and Geology.

Hammersley, L. & DePaolo, D. J. (2006). Isotopic and geophysical constraints on the structure and evolution of the Clear Lake volcanic system. *Journal of Volcanology and Geothermal Research* **153**, 331–356.

Hanson, R. B., Sorensen, S. S., Barton, M. D. & Fiske, R. S. (1993). Long-term evolution of fluid–rock interactions in magmatic arcs: evidence from the Ritter range pendant, Sierra Nevada, California and numerical modeling. *Journal of Petrology* **34**, 23–62.

Henyey, T. L. & Lee, T.-C. (1976). Heat flow in Lake Tahoe, California–Nevada, and the Sierra Nevada–Basin and Range transition. *Geological Society of America Bulletin* **87**, 1179–1187.

Hofmann, A. W. (1988). Chemical differentiation of the Earth: the relationship between mantle, continental crust, and oceanic crust. *Earth and Planetary Science Letters* **90**, 297–314.

Kerrick, D. M. (1970). Contact metamorphism in some areas of the Sierra Nevada, California. *Geological Society of America Bulletin* **81**, 2913–2938.

Kerrick, D. M. (1977). The genesis of zoned skarns in the Sierra Nevada, California. *Journal of Petrology* **18**, 144–181.

Kistler, R. W., Bateman, P. C. & Brannock, W. W. (1965). Isotopic ages of minerals from granitic rocks of the Central Sierra Nevada and Inyo Mountains, California. *Geological Society of America Bulletin* **76**, 155–164.

Lachenbruch, A. H. (1968). Preliminary geothermal model of the Sierra Nevada. *Journal of Geophysical Research* **73**, 6977–6989.

Lackey, J. S. & Valley, J. W. (2004). Complex patterns of fluid flow during wollastonite formation in calcareous sandstones at Laurel Mountain, Mmt. Morrison Pendant, California. *Geological Society of America Bulletin* **116**, 76–93.

Lackey, J. S., Valley, J. W., Chen, J. H. & Stockli, D. F. (2008). Dynamic magma systems, crustal recycling, and alteration in the central Sierra Nevada batholith: the oxygen isotope record. *Journal of Petrology* **49**, 1397–1426.

Lee, C.-T., Rudnick, R. L. & Brimhall, G. H. (2001). Deep lithospheric dynamics beneath the Sierra Nevada during the Mesozoic and Cenozoic as inferred from xenolith petrology. *Geochemistry, Geophysics, Geosystems* **2**, 2001GC000152.

Lee, C.-T. A., Cheng, X. & Horodyskyj, U. (2006). The development and refinement of continental arcs by primary basaltic magmatism, garnet pyroxenite accumulation, basaltic recharge and delamination: insights from the Sierra Nevada, California. *Contributions to Mineralogy and Petrology*, doi:10.1007/s00410-00005-00056-00411.

Lee, C.-T. A., Morton, D. M., Kistler, R. W. & Baird, A. K. (2007). Petrology and tectonics of Phanerozoic continent formation: from island arcs to accretion and continental arc magmatism. *Earth and Planetary Science Letters* **263**, 370–387.

Lee, C.-T. A., Luffi, P., Plank, T., Dalton, H. A. & Leeman, W. P. (2009*a*). Constraints on the depths and temperatures of basaltic magma generation on Earth and other terrestrial planets using new thermobarometers for mafic magmas. *Earth and Planetary Science Letters* **279**, 20–33.

Lee, C.-T. A., Oka, M., Luffi, P. & Agranier, A. (2009*b*). Internal distribution of Li and B in serpentinites from the Feather River Ophiolite, California based on laser ablation inductively coupled plasma mass spectrometry. *Geochemistry, Geophysics, Geosystems* **9**, doi:10.1029/2008GC002078.

Lesher, C. E. (1990). Decoupling of chemical and isotopic exchange during magma mixing. *Nature* **344**, 235–237.

Lindgren, W. (1933). *Mineral Deposits*. New York: McGraw–Hill.

Liu, Y., Zhang, Y. & Behrens, H. (2005). Solubility of H_2O in rhyolitic melts at low pressures and a new empirical model for mixed H_2O–CO_2 solubility in rhyolitic melts. *Journal of Volcanology and Geothermal Research* **143**, 219–235.

Longerich, H. P., Jackson, S. E. & Gunther, D. (1996). Laser ablation inductively coupled plasma mass spectrometric transient signal data acquisition and analyte concentration calculation. *Journal of Analytical Atomic Spectrometry* **11**, 899–904.

Martel, S. J., Harrison, T. M. & Gillespie, A. R. (1987). Late Quaternary vertical displacement rate across the Fish Springs fault, Owens Valley fault zone, California. *Quaternary Research* **27**, 113–129.

McDonough, W. F. & Sun, S.-S. (1995). The composition of the Earth. *Chemical Geology* **120**, 223–253.

Miller, R. H. (1975). Late Ordovican–Early Silurian conodont biostratigraphy, Inyo Mountains, California. *Geological Society of America Bulletin* **86**, 159–162.

Mills, R. D., Glazner, A. F. & Coleman, D. R. (2009). Scale of pluton/wall-rock interaction near May Lake, Yosemite National Park, CA, USA. *Contributions to Mineralogy and Petrology* **158**, 263–281.

Moore, J. N. & Foster, C. T., Jr (1980). Lower Paleozoic metasedimentary rocks in the east–central Sierra Nevada, California: correlation with Great Basin formations. *Geological Society of America Bulletin* **91**, 37–43.

Mordick, B. E. & Glazner, A. F. (2006). Clinopyroxene thermobarometry of basalts from the Coso and Big Pine volcanic fields. *Contributions to Mineralogy and Petrology* **152**, 111–124.

Nelson, C. A. (1966). Geologic map of the Waucoba Mountain quadrangle, Inyo County, Californnia. *US Geological Survey Geologic Quadrangle Series* **528.**

Newman, S. & Lowenstern, J. B. (2002). VC: a silicate melt–H_2O–CO_2 solution model written in Visual Basic for Excel. *Computers and Geosciences* **28**, 597–604.

Ormerod, D. S., Hawkesworth, C. J., Rogers, N. W., Leeman, W. P. & Menzies, M. A. (1988). Tectonic and magmatic transitions in the Western Great Basin, USA. *Nature* **333**, 349–353.

Pickett, D. A. & Saleeby, J. B. (1993). Thermobarometric constraints on the depth of exposure and conditions of plutonism and metamorphism at deep levels of the Sierra Nevada Batholith, Tehachapi Mountains, California. *Journal of Geophysical Research* **98**, 609–629.

Ratajeski, K., Glazner, A. F. & Miller, B. V. (2001). Geology and geochemistry of mafic to felsic plutonic rocks associated with the Cretaceous intrusive suite of Yosemite Valley, California. *Geological Society of America Bulletin* **113**, 1486–1502.

Satish-Kumar, M., Yoshida, Y. & Kusachi, I. (2004). The role of aqueous silica concentration in controlling the mineralogy during high temperature contact metamorphism: a case study from Fuka contact aureole, Okayama, Japan. *Journal of Mineralogical and Petrological Sciences* **99**, 328–338.

Sawka, W. N., Chappell, B. W. & Kistler, R. W. (1990). Granitoid compositional zoning by side-wall boundary layer differentiation: evidence from the Palisade Crest Intrusive suite, central Sierra Nevada, California. *Journal of Petrology* **31**, 519–553.

Spera, F. J. & Bohrson, W. A. (2001). Energy-constrained open-system magmatic processes I: general model and energy-constrained assimilation and fractional crystallization (EC-AFC) formulation. *Journal of Petrology* **42**, 999–1018.

Sylvester, A. G. (1969). SA microfabric study of calcite, dolomite, and quartz around Papoose Flat pluton, California. *Geological Society of America Bulletin* **80**, 1311–1328.

van Marcke de Lummen, G. & Verkaeren, J. (1986). Physicochemical study of skarn formation in pelitic rock, Costabonne peak area, eastern Pyrenees, France. *Contributions to Mineralogy and Petrology* **93**, 77–88.

Wang, K., Plank, T., Walker, J. D. & Smith, E. I. (2002). A mantle melting profile across the Basin and Range, SW USA. *Journal of Geophysical Research* **107(1)**, 21.

Wark, D. A. & Watson, E. B. (2006). TitaniQ: a titanium-in-quartz geothermometer. *Contributions to Mineralogy and Petrology* **152**, 743–754.

Woodford, D. T., Sisson, V. B. & Leeman, W. P. (2001). Boron metasomatism of the Alta stock contact aureole, Utah: evidence from borates, mineral chemistry, and geochemistry. *American Mineralogist* **86**, 513–533.

Wright, L., Williams, E. G. & Cloud, P. (1978). Algal and cryptalgal structures and platform environments of the late pre-Phanerozoic Noonday dolomite, eastern California. *Geological Society of America Bulletin* **89**, 321–333.

Zehfuss, P. H., Bierman, P. R., Gillespie, A. R., Burke, R. M. & Caffee, M. W. (2001). Slip rates on the Fish Springs fault, Owens Valley, California, deduced from cosmogenic ^{10}Be and ^{26}Al and soil development on fan surfaces. *Geological Society of America Bulletin* **113**, 241–255.